

# The mass of the exo-Venus Gliese 12 b, as revealed by HARPS-N, ESPRESSO, and CARMENES

Daisy A. Turner<sup>1\*</sup>, Yoshi Nike Emilia Eschen<sup>2</sup>, Felipe Murgas<sup>3,4</sup>, Annelies Mortier<sup>1</sup>, Thomas G Wilson<sup>2</sup>, Jorge Fernández Fernández<sup>2</sup>, Giuseppe Morello<sup>5,6</sup>, Shreyas Vissapragada<sup>7</sup>, José A. Caballero<sup>8</sup>, Stefan Dreizler<sup>9</sup>, Jo Ann Egger<sup>10</sup>, Alix Violet Freckelton<sup>1</sup>, Nicole Gromek<sup>11</sup>, Artie P. Hatzes<sup>12</sup>, Ben Scott Lakeland<sup>1</sup>, Evangelos Nagel<sup>9</sup>, Luca Naponiello<sup>13</sup>, Hugo M. Tabernero<sup>14,15</sup>, Siegfried Vanaverbeke<sup>16,17</sup>, Alexander Venner<sup>18</sup>, María Rosa Zapatero Osorio<sup>8</sup>, Pedro J. Amado<sup>5</sup>, Víctor J. S. Béjar<sup>3,4</sup>, Aldo Stefano Bonomo<sup>13</sup>, Lars A. Buchhave<sup>19</sup>, Andrew Collier Cameron<sup>20</sup>, Ilaria Carleo<sup>13</sup>, Priyanka Chaturvedi<sup>12,21</sup>, Ryan Cloutier<sup>11</sup>, Mario Damasso<sup>13</sup>, Mangesh Daspute<sup>22</sup>, Shishir Dholakia<sup>18</sup>, Sjoerd Dufoer<sup>16</sup>, Xavier Dumusque<sup>23</sup>, Aldo Fabricio Martinez Fiorenzano<sup>24</sup>, Adriano Ghedina<sup>24</sup>, Avet Harutyunyan<sup>24</sup>, Enrique Herrero<sup>15</sup>, Ancy Anna John<sup>1</sup>, Jorge Lillo-Box<sup>8</sup>, Nicolas Lodieu<sup>3,4</sup>, Mercedes López-Morales<sup>25</sup>, Luca Malavolta<sup>26,27</sup>, Luigi Mancini<sup>28</sup>, Giacomo Mantovan<sup>26,27</sup>, David Montes<sup>29</sup>, Juan Carlos Morales<sup>14,15</sup>, Belinda Nicholson<sup>18</sup>, Jaume Orell-Miquel<sup>30</sup>, Larissa Palethorpe<sup>31,32</sup>, Enric Palle<sup>3,4</sup>, Andreas Quirrenbach<sup>33</sup>, Sabine Reffert<sup>33</sup>, Ansgar Reiners<sup>9</sup>, Ignasi Ribas<sup>14,15</sup>, Ken Rice<sup>31,32</sup>, André M. Silva<sup>34,35</sup>, Alessandro Sozzetti<sup>13</sup>, Manu Stalport<sup>36,37</sup>, Lev Tal-Or<sup>22,38</sup>, Trifon Trifonov<sup>33,39</sup>, Stéphane Udry<sup>23</sup>, Mathias Zechmeister<sup>9</sup>

*Affiliations are listed at the end of the paper*

Accepted XXX. Received YYY; in original form ZZZ

## ABSTRACT

Small temperate planets are prime targets for exoplanet studies due to their possible similarities with the rocky planets in the Solar System. M dwarfs are promising hosts since the planetary signals are within our current detection capabilities. Gliese 12 b is a Venus-sized temperate planet orbiting a quiet M dwarf. We present here the first precise mass measurement of this small exoplanet. We performed a detailed analysis using HARPS-N, ESPRESSO, and CARMENES radial velocities, along with new and archival *TESS*, *CHEOPS*, and *MuSCAT2/3* photometry data. From fitting the available data, we find that the planet has a radius of  $R_p = 0.904^{+0.037}_{-0.034} R_\oplus$  and a mass of  $M_p = 0.95^{+0.26}_{-0.27} M_\oplus$  (a  $3.6\sigma$  measurement of the semi-amplitude  $K = 0.70^{+0.19}_{-0.20} \text{ m s}^{-1}$ ), and is on an orbit with a period of  $12.761421 \pm 0.000047 \text{ d}$ . A variety of techniques were utilised to attenuate stellar activity signals. Gliese 12 b has an equilibrium temperature of  $T_{\text{eq}} = 315 \pm 7 \text{ K}$ , assuming an albedo of zero, and a density consistent with that of Earth and Venus ( $\rho_p = 7.0^{+2.3}_{-2.1} \text{ g cm}^{-3}$ ). We find that Gliese 12 b has a predominantly rocky interior and simulations indicate that it is unlikely to have retained any of its primordial gaseous envelope. The bulk properties of Gliese 12 b place it in an extremely sparsely-populated region of both mass–radius and density– $T_{\text{eq}}$  parameter space, making it a prime target for follow-up observations, including Lyman- $\alpha$  studies.

**Key words:** planets and satellites: detection – planets and satellites: terrestrial planets – planets and satellites: interiors – techniques: radial velocities – stars: individual: Gliese 12 – planets and satellites: individual: Gliese 12 b

## 1 INTRODUCTION

One of the principal motivators in the field of exoplanetary science is the desire to find planets that are analogous to Earth or other small Solar System planets, in size, mass, composition, and potential habitability. M dwarfs have emerged as especially promising targets, as their relatively low masses and radii facilitate the detection of small planets. Their habitable zones also lie closer in, meaning potentially habitable planets are on more detectable orbits. While there could

be drawbacks with habitability for planets hosted by M dwarfs (e.g. lower UV flux, tidal locking), the possibility of life is not ruled out for these planets (see [Shields et al. 2016](#), for a review).

Significant progress has been made in identifying small planets, primarily through large surveys. Since the first light of pioneering telescopes such as *CoRoT* (CONvection, ROTation and planetary Transits; [Baglin 2003](#)) and *Kepler* ([Borucki et al. 2010](#)), the detection of exoplanets has undergone a revolution, resulting in a dramatic increase in the rate of discoveries. These missions have demonstrated that small planets (here loosely defined as any planet with a radius

\* E-mail: dat936@student.bham.ac.uk

smaller than  $2 R_{\oplus}$ ) are abundant, particularly around M dwarfs (e.g., Dressing & Charbonneau 2015; Sabotta et al. 2021).

As of May 2025, around 6000 exoplanets have been detected,<sup>1</sup> with thousands of other targets identified as exoplanetary candidates, evidencing the vital part that space-based surveys play in establishing a selection of targets for follow-up. However, while these missions have revealed many small planets, the understanding of this population is incomplete without measurements of their masses.

Obtaining precise planetary mass measurements remains challenging and time consuming. This is especially true for planets with radial velocity (RV) semi-amplitudes of less than  $1 \text{ m s}^{-1}$  (e.g., Pepe et al. 2011; Wilson et al. 2022; Stalport et al. 2025), a regime characteristic of Earth-mass planets around M dwarfs (e.g., Demangeon et al. 2021; Bonomo et al. 2023; Murgas et al. 2023; Basant et al. 2025). Such signals are further obscured by stellar activity, a considerable source of noise that is typically pronounced for faint M dwarfs such as Gliese 12. To achieve the precision necessary to characterise Earth-mass planets, data from high-resolution spectrographs, such as HARPS-N (High Accuracy Radial velocity Planet Searcher for the Northern Hemisphere; Cosentino et al. 2012), ESPRESSO (Echelle Spectrograph for Rocky Exoplanets and Stable Spectroscopic Observations; Pepe et al. 2014, 2021), and CARMENES (Calar Alto high-Resolution search for M dwarfs with Exoearths with Near-infrared and optical Echelle Spectrographs; Quirrenbach et al. 2014, 2018), are required.

Currently, very few Earth-sized planets have both precise masses and radii. This small sample of planets acts as a critical benchmark to understand planet composition, formation, evolution, and habitability. With measurements of both radius and mass, the bulk density of a planet can be calculated, allowing for an understanding of its approximate interior structure and composition. We can furthermore use the mass and radius to simulate scenarios for the atmospheric evolution of a planet and infer its prospects for atmospheric characterisation with, e.g., *JWST* or *HST*. With more planetary information available, a planet’s similarity to Solar System planets can more easily be gauged.

The transit of Gliese 12 b was discovered by *TESS* (TOI-6251), and using separate validation data, Dholakia et al. (2024) and Kuzuhara et al. (2024) announced the validation of this planet. Gliese 12 b is a planet with a radius close to  $1 R_{\oplus}$ , putting it firmly in the Earth-like regime. It orbits its host star every  $\sim 12.76$  d. Since Gliese 12 is an M dwarf, this puts the planet in the habitable zone where liquid water is sustained at the surface.

While Dholakia et al. (2024) and Kuzuhara et al. (2024) did use RV measurements to validate the planet, its mass remained unmeasured due to an insufficient amount of data. This left key aspects unconstrained, such as its density, composition and potential for life. In this study, we present the first mass measurement of Gliese 12 b using extremely-precise RVs from three spectrographs: HARPS-N, ESPRESSO and CARMENES.

In Section 2, we describe the data sets used in this work. This includes both photometry and spectroscopy. The host star and its properties are described in Section 3. We performed an individual photometry fit, an RV fit informed by the photometry fit and a joint fit, all of which are described in Sections 4, 5, and 6. Finally, we discuss the implications of this new mass measurement in Section 7 and conclude in Section 8.

## 2 DATA

### 2.1 Photometry

Gliese 12 has been observed extensively, as described by Dholakia et al. (2024) and Kuzuhara et al. (2024). In this work, we use transit data from *TESS*, *CHEOPS*, MuSCAT2, MuSCAT3, and long-term photometry from ASAS-SN, LCOGT, TJO, and E-EYE.

#### 2.1.1 TESS

The Transiting Exoplanet Survey Satellite (*TESS*; Ricker et al. 2015; Ricker 2021) has observed Gliese 12 in a total of five sectors, each being approximately 27 d long. Four of these sectors were previously presented by Dholakia et al. (2024), totalling around 135 d of coverage. The orbital period of Gliese 12 b was initially ambiguous, as the first few sectors of *TESS* data were consistent with periods of 12.76 or 25.52 d. Ultimately, in sectors 42, 43, 57, and 70, a total of five transits were identified, leading to the confirmation of a planetary orbital period of  $\sim 12.76$  d.

Gliese 12 was observed again in *TESS* sector 84, the first sector of Cycle 7, between 2024 October 01 and 2024 October 26 (BJD 2460584.50 – BJD 2460609.50). These data were released after the publication of Dholakia et al. (2024), and 2 additional transits events were captured. These data were taken using CCD 3 on camera 1. In all, the data span approximately 105 d.

We have used the PDCSAP data, downloaded from the MAST portal<sup>2</sup>.

#### 2.1.2 CHEOPS

The CHAracterising ExOPlanet Satellite (*CHEOPS*; Benz et al. 2021) is a follow-up mission launched in 2019 with the goal to derive radii of planets more precisely. Dholakia et al. (2024) presented five *CHEOPS* visits of the transits of Gliese 12 b which were obtained in the *CHEOPS* AO-4 guest observers programmes with the IDs ID:07 (PI: Palethorpe) and ID:12 (PI: Venner). Since then an additional visit has been obtained within the ID:12 programme and a transit observed. The six available *CHEOPS* visits are summarised in Table 1.

As Gliese 12 is a rather faint target to be observed by *CHEOPS*, we re-extract the photometry using the PSF Imagette Photometric Extraction (PIPE; Brandeker et al. 2024) instead of the aperture photometry produced by *CHEOPS*’ Data Reduction Pipeline (DRP; Hoyer et al. 2020). We analysed each visit individually using *pycheops* (Maxted et al. 2022) and *juliet* (Espinoza et al. 2019), a planet modelling tool using nested sampling and implementing *batman* (Kreidberg 2015) to model the transits. We obtained the detrending vectors for each *CHEOPS* visit in *pycheops* via Bayes Factor assessments of simultaneously fitting subsets of the detrending vectors with a transit model. We subsequently detrended the visits using linear regressors in *juliet*. The detrended vectors for each visit are reported in Table 1. We also applied a  $3\sigma$ -clipping to the data, removing outliers that were more than  $3\sigma$  away from the mean of the data.

We note that there are an additional four opportunistic *CHEOPS* visits available from 2020 September 22 to 2021 September 19. However, since these do not cover any transits, we did not include these in any further analysis.

<sup>1</sup> <https://exoplanetarchive.ipac.caltech.edu>

<sup>2</sup> <https://mast.stsci.edu/>

**Table 1.** Summary of the *CHEOPS* observations of Gliese 12 and the used detrending vectors.

Visit	Start Date (UTC)	Duration (h)	Data Points (#)	File Key	Efficiency (%)	Exp Time (s)	Detrending Vectors
1	2023-09-24T00:03:43	11.41	513	CH_PR240007_TG000101	74.9	60	t, x, y <sup>2</sup>
2	2023-10-06T18:19:43	12.76	481	CH_PR240007_TG000102	62.8	60	-
3	2023-10-19T16:32:43	6.80	222	CH_PR240012_TG000701	54.3	60	-
4	2023-11-14T06:29:42	6.92	241	CH_PR240012_TG000702	57.9	60	-
5	2023-11-26T21:38:42	7.44	248	CH_PR240012_TG000101	55.5	60	x, t, cos(2 $\phi$ )
6	2024-08-20T23:26:43	6.47	279	CH_PR240012_TG000801	71.7	60	smear, contam

### 2.1.3 *MuSCAT*

As presented by [Kuzuhara et al. \(2024\)](#), two transits of Gliese 12 b have been observed with *MuSCAT2* ([Narita et al. 2019](#)) and two transits with *MuSCAT3* ([Narita et al. 2020](#)). Directly following the method of [Kuzuhara et al. \(2024\)](#), we detrended the data using a Gaussian Process (GP) regression with a Matérn 3/2 kernel. Similar to our approach with the *CHEOPS* data, we performed this detrending for each visit separately.

### 2.1.4 *ASAS-SN*

We downloaded all the available data from the All-Sky Automated Survey for Supernovae (*ASAS-SN*; [Shappee et al. 2014](#); [Kochanek et al. 2017](#)). There are 213 *V* band observations taken from 2013 December 5 till 2018 November 29. We removed three outliers via 5-MAD clipping leaving us with 210 data points taken over 207 epochs. The RMS of the data is half the median error, confirming that this is a quiet star.

### 2.1.5 *LCOGT*

We obtained photometric observations with the Las Cumbres Observatory Global Telescope (*LCOGT*; [Brown et al. 2013](#)). The target star was observed using the 0.4 m and 1.0 m telescopes in the *V* and *B* bands, respectively. For the *B*-band observations, we used an exposure time of 30 s and collected a total of 570 images between 2023 December 14 and 2025 January 16. For the *V* band, the exposure time was 300 s, and we collected 241 images between 2024 August 24 and 2024 December 26. The images were calibrated using the standard *LCOGT* BANZAI pipeline ([McCully et al. 2018](#)), and differential photometry was extracted with *AstroImageJ* ([Collins et al. 2017](#)).

### 2.1.6 *TJO*

A long-term photometric campaign of Gliese 12 was carried out using the 0.8 m Joan Oró Telescope (*TJO*; [Colomé et al. 2010](#)) at the Montsec Observatory in Lleida, Spain. We obtained a total of 1106 *R*-band images between 2023 May 23 and 2025 January 09. The raw science images were calibrated using the *ICAT* pipeline ([Colomé & Ribas 2006](#)).

**Table 2.** Summary of the RV observations.

Instrument	Number of RVs	Average error (m s <sup>-1</sup> )	Standard deviation (m s <sup>-1</sup> )
HARPS-N	76 (74)	1.43 (1.43)	2.88 (2.90)
ESPRESSO	35 (34)	0.35 (0.35)	1.90 (1.92)
CARMENES	93 (91)	1.77 (1.77)	3.38 (2.47)

Notes: Values enclosed in brackets are calculated from data after outliers are excluded. For HARPS-N and ESPRESSO, the S-BART values were used.

### 2.1.7 *E-EYE*

We collected data with *e-EYE*<sup>3</sup> (short for ‘Entre Encinas y Estrelas’), a 16-inch Optimised Dall-Kirkhams (ODK) reflector located at Fregenal de la Sierra in Badajoz, Spain. A total of 351 images were obtained: 175 in the *V* band and 176 in the *R* band. The observations span the period from 2023 December 14 to 2025 February 25. Image reduction and differential aperture photometry of the target and several reference stars were performed using the *LesvePhotometry* package<sup>4</sup>.

## 2.2 Spectroscopy

In this work, we use three different spectroscopic data sets, taken by HARPS-N, ESPRESSO, and CARMENES. There is also the publicly available data from IRD used in [Kuzuhara et al. \(2024\)](#). We decided not to use the latter due to the difference in scatter as compared to the more stabilised data used in this work. Outliers within each used dataset were removed (post-re-extraction in the case of HARPS-N and ESPRESSO) via identifying data points with uncertainties more than  $3\sigma$  from the median uncertainty on an instrument-by-instrument basis. Summary statistics on the RVs are mentioned in Table 2, and the full set of RVs used in our analyses are shown in Figure 1.

### 2.2.1 *HARPS-N*

We obtained 87 observations with the HARPS-N spectrograph ([Cosentino et al. 2012](#)), a small subset of which was already published in [Dholakia et al. \(2024\)](#). HARPS-N is a high-precision, high-resolution echelle spectrograph installed on the Telescopio Nazionale Galileo (TNG) in La Palma, Spain. The instrument covers a wavelength range of 383–693 nm and has an average resolving power

<sup>3</sup> <https://www.e-eye.es/>

<sup>4</sup> <http://www.dppobservatory.net/>

of  $\mathcal{R} = 115\,000$ . Observations were taken over four semesters, from 2023 August 09 to 2025 January 28 (BJD 2460165.66 – BJD 2460704.35), spanning just under a year and a half. 13 observations were obtained via the Guaranteed Time Observation (GTO) programme, with the remaining data collected as part of the HARPS-N Collaboration under programme A48TAC\_59 (PI: L. Malavolta).

The target was observed with the second fibre pointed at the sky, with observations having an average exposure time of 1800 s. The data were processed with the standard HARPS-N DRS (Data Reduction Software – version 3.0.1 – Dumusque et al. (2021)), with an M5 mask used to obtain the Cross Correlation Functions (CCFs). Additionally, the DRS calculated several spectral activity indicators, including the S-index and H  $\alpha$  metric from the spectra. The median SNR in order 50 is 24.

To ensure homogeneity across all instruments, and accounting for the specific CCF shape of M dwarfs, activity indicators were re-extracted from the CCFs following Lafarga et al. (2020). An inverted Gaussian was fit to the CCF, from which the contrast, full width at half maximum (FWHM), and bisector inverse slope (BIS) were calculated. To obtain the BIS values, we followed the method outlined by Queloz et al. (2001), where the top and bottom regions of the CCF are defined as the sections between 60 and 90 per cent, and 10 and 40 per cent, respectively.

As Gliese 12 is an M dwarf, obtaining RVs using the CCF method is challenging due to the large number of spectral lines and their blending. Hence, we re-extracted the RVs using the Semi-Bayesian Approach for RVs with Template-matching<sup>5</sup> (S-BART; Silva et al. 2022) which is shown to be especially successful in its application to M-dwarfs. Within this process, we re-extracted RVs for different quality checks including all combinations of RV steps (0.1, 0.5, 1.0 m s<sup>-1</sup>), RV limits (200, 500, 1000 m s<sup>-1</sup>), minimum order signal-to-noise ratio (S/N; 1.5, 5, 10), airmasses (1.5, 2.0, 2.2, 2.6) and RV errors (5, 6, 7, 10 m s<sup>-1</sup>) as well as the classical and Laplacian method S-BART applies. We selected the re-extracted RVs producing the lowest median error in S-BART. These are for an RV step of 0.1 m s<sup>-1</sup>, RV limit of 500 m s<sup>-1</sup>, minimum order S/N of 1.5, airmass of 1.5 and RV errors of 5 m s<sup>-1</sup>. We selected the RVs reprocessed using the Laplacian method. This removed 11 data points whose spectra did not fulfil S-BART’s quality checks and left 76 HARPS-N RVs. The median error of the RVs in S-BART was reduced to 1.43 m s<sup>-1</sup> as compared to 2.98 m s<sup>-1</sup> from the DRS. The standard deviation of the RVs became 2.88 m s<sup>-1</sup> from S-BART compared to 5.10 m s<sup>-1</sup> from the DRS.

### 2.2.2 ESPRESSO

Gliese 12 was observed with ESPRESSO (Pepe et al. 2014, 2021), a high-resolution echelle spectrograph installed at the incoherent combined coudé facility of the Very Large Telescope (VLT) at the Paranal Observatory, Chile. ESPRESSO is ultra-stable, covers a wavelength range of 380–788 nm and has an average resolving power of  $\mathcal{R} = 140\,000$ . A total of 35 observations were taken between 2024 June 06 to 2024 September 23 (BJD 2460467.90 – BJD 2460576.75) as part of a Cycle P113 programme with ID:113.26RH (PI: Thomas G. Wilson). With an exposure time of 1200 s, we obtained a median SNR at  $\sim 550$  nm of 29.50. The data were processed through the standard ESPRESSO DRS (version 3.3.1) with an M5 mask. Similar to the HARPS-N data, this produced CCFs as well as spectral activity indicators.

We again re-processed the RVs using S-BART for all the combinations of quality checks stated above. We also select the quality check combination producing RVs with the lowest median error of 0.35 m s<sup>-1</sup> compared to a median error of 0.70 m s<sup>-1</sup> from the DRS. This results in a standard deviation of 1.90 m s<sup>-1</sup> for S-BART and 2.14 m s<sup>-1</sup> for the DRS. For ESPRESSO this is the case for an RV step of 0.1 m s<sup>-1</sup>, RV limit of 200 m s<sup>-1</sup>, minimum order S/N of 1.5, airmass of 1.5 and RV error of 7 m s<sup>-1</sup> as well as applying the Laplacian method in S-BART. This method keeps in all 35 RV observations taken by ESPRESSO. The RVs utilised in our analyses were those extracted using S-BART.

### 2.2.3 CARMENES

Gliese 12 was observed with the CARMENES spectrograph installed at the 3.5 m telescope of Calar Alto Observatory in Almeria, Spain. CARMENES has two channels, one operating at visible wavelengths (VIS, spectral range 0.52–0.96  $\mu\text{m}$ ) and one operating at near-infrared wavelengths (NIR, spectral range 0.96–1.71  $\mu\text{m}$ ). The average spectral resolution of the VIS channel is  $\mathcal{R} = 94\,600$  and the resolution of the NIR channel is  $\mathcal{R} = 80\,400$  (Quirrenbach et al. 2014, 2018).

A total of 93 RV measurements were collected from 2023 June 28 to 2025 January 15 (BJD 2460123.59 – BJD 2460691.34), and part of the data collected in 2023 was presented in Kuzuhara et al. (2024). The spectra were acquired with an exposure time of 1800 s. Data reduction was performed using the CARACAL pipeline (Caballero et al. 2016), which applies standard corrections for bias, flat field, and cosmic rays, and extracts spectra using the FOX optimal extraction algorithm (Zechmeister et al. 2014). Wavelength calibration was carried out following the procedure described by Bauer et al. (2015). RV measurements were obtained with the template-matching algorithm SERVAL<sup>6</sup> (Zechmeister et al. 2018). The RV measurements were corrected for other effects such as barycentric motion, secular acceleration, instrumental drifts, and nightly zero-points (e.g., Trifonov et al. 2018; Tal-Or et al. 2018).

The 93 spectra have a median S/N of 90 measured at the spectral order centred at 746 nm (minimum S/N = 27, maximum S/N = 118) in the VIS channel. The median value of the RV uncertainties are 1.76 m s<sup>-1</sup> for the VIS channel, and 6.24 m s<sup>-1</sup> for the NIR channel. In this work, we use only the VIS channel RVs, as they present significantly lower scatter than the NIR velocities.

## 3 HOST STAR CHARACTERISATION

Gliese 12 is a nearby metal-poor M dwarf, likely belonging to the Galactic thin disc; see Dholakia et al. (2024) for a discussion of the kinematics.

It was extensively characterised by Dholakia et al. (2024) and Kuzuhara et al. (2024). Their parameters are easily consistent with errors. We choose to mainly use the parameters from Kuzuhara et al. (2024) as these include more individual chemical abundances which are later used to model the interior composition of Gliese 12 b. The relevant values are summarised in Table 3.

<sup>5</sup> <https://github.com/iastro-pt/sBART>

<sup>6</sup> <https://github.com/mzechmeister/serval>

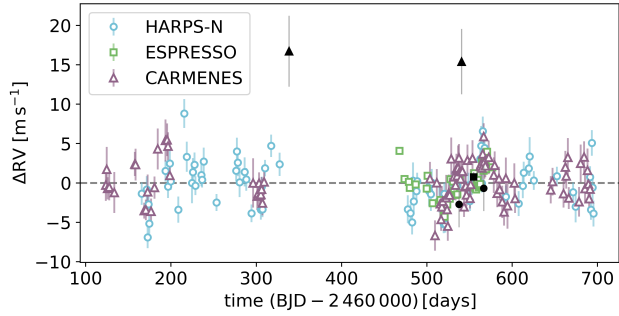


**Figure 1.** Gliese 12 RVs with offsets removed; HARPS-N, ESPRESSO, and CARMENES data are plotted as blue circles, green squares, and purple triangles, respectively. Uncertainties on the ESPRESSO RVs are smaller than the marker points. Outliers are indicated by the black markers.

**Table 3.** Gliese 12 stellar parameters used in this work.

Parameter	Unit	Value	Source
$T_{\text{eff}}$	(K)	$3296^{+48}_{-36}$	(1)
$M_{\star}$	( $M_{\odot}$ )	$0.2414 \pm 0.0060$	(1)
$R_{\star}$	( $R_{\odot}$ )	$0.2617^{+0.0058}_{-0.0070}$	(1)
$\rho_{\star}$	( $\rho_{\odot}$ )	$13.5^{+1.2}_{-0.9}$	(1)
Age	(Gyr)	$7.0^{+2.8}_{-2.2}$	(2)
Distance	(pc)	$12.1616^{+0.0051}_{-0.0053}$	(3)
[Fe/H]	(dex)	$-0.32 \pm 0.06$	(1)
[Mg/H]	(dex)	$-0.32 \pm 0.22$	(1)
$P_{\text{rot}}$	(d)	$\sim 85$	(1), (4)
$\langle \log R'_{\text{HK}} \rangle$	—	$-5.62^{+0.10}_{-0.14}$	(4)

Notes: (1) Kuzuhara et al. (2024), (2) Dholakia et al. (2024), (3) Bailer-Jones et al. (2021), (4) This work

### 3.1 Stellar variability

Gliese 12 is overall a very quiet star as evidenced by its low  $\langle \log R'_{\text{HK}} \rangle$  value, a low X-ray flux, and low variability in the photometry.

We recalculated the  $\langle \log R'_{\text{HK}} \rangle$  from the HARPS-N spectra and following the expressions of Astudillo-Defru et al. (2017). We found that over the timespan of the data,  $\langle \log R'_{\text{HK}} \rangle = -5.62$ . Using the estimated relation between  $\langle \log R'_{\text{HK}} \rangle$  and the rotation period from Astudillo-Defru et al. (2017), the median rotation period is predicted to be  $\sim 75$  d.

We attempted to determine the stellar rotation period of Gliese 12 using long-term, ground-based photometric data from ASAS-SN, LCOGT, TJO, and E-EYE (see Fig. A1). Each dataset was analysed independently — except for the E-EYE data, which included simultaneous  $V$  and  $R$  observations on the same nights — to assess whether they yielded consistent estimates of  $P_{\text{rot}}$ . To model the photometric time series, we fitted a linear function to account for long-term trends, alongside a sinusoidal function:

$$f(t) = z + mt + A \sin\left(\frac{2\pi t}{P_{\text{rot}}} + \phi\right). \quad (1)$$

Here,  $t$  denotes the epoch of the photometric measurements. The free parameters include  $z$  and  $m$ , the coefficients of the linear trend, and the sinusoidal components: amplitude  $A$ , rotation period  $P_{\text{rot}}$ ,

**Table 4.** Stellar rotation estimates from long-term photometry.

Facility	Photometric band	Value
ASAS-SN	$g$	$P_{\text{rot}} = 85.2^{+0.4}_{-0.3}$ d
LCOGT	$B$	$P_{\text{rot}} = 92.7^{+4.8}_{-2.9}$ d
LCOGT	$V$	$P_{\text{rot}} = 86.6^{+22.3}_{-32.5}$ d
TJO	$R$	$P_{\text{rot}} = 77.0^{+1.9}_{-1.9}$ d
E-EYE	$V, R$	$P_{\text{rot}} = 81.8^{+3.3}_{-3.2}$ d

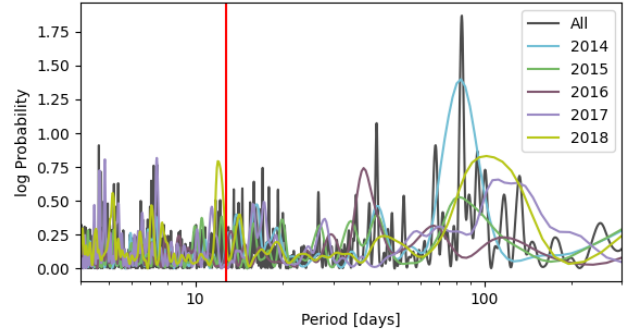


**Figure 2.** BGLS periodogram of the ASAS-SN data of Gliese 12, of the full data and per season. The red vertical line indicates the planet period.

and phase  $\phi$ . To account for systematic effects in the data, we employed GPs (e.g., Rasmussen & Williams 2010; Gibson et al. 2012), specifically using an exponential kernel implemented in Celerite<sup>7</sup> (Foreman-Mackey et al. 2017). We ran PyDE<sup>8</sup> to find optimal initial solutions, followed by a Markov chain Monte Carlo (MCMC) analysis with emcee (Foreman-Mackey et al. 2013) to determine posterior distributions (50 chains,  $2 \times 10^4$  iterations with a thin factor of 100). Final parameter values were derived from these, using the median and  $1\sigma$  percentiles.

The derived  $P_{\text{rot}}$  values are listed in Table 4. Our results indicate a relatively long stellar rotation period, with most estimates falling in the 80–90 day range. The most precise determination comes from the ASAS-SN data, yielding  $P_{\text{rot}} = 85.2^{+0.4}_{-0.3}$  d. Applying a BGLS periodogram (Mortier et al. 2015) and splitting the data into the five different observing seasons, we found that this signal is strongest only in 2014, where the other years show mostly insignificant variation at a multitude of periods. The periodogram is shown in Figure 2. It confirms that this star is relatively quiet and that there is (unsurprisingly) inter-seasonal variability. We caution that this may artificially lower the errors on the derived rotation period above.

Finally, we looked at the discrete correlation function (DCF) between  $H\alpha$  and RVs. Since these are measured from the same spectra and available for all our spectroscopic data sets, they could be used in a multi-dimensional GP regression fit. We apply the algorithm from Edelson & Krolik (1988) to compute the DCF. The resulting analysis shows that  $H\alpha$  and RVs are mildly anti-correlated and that there is a small timeshift of about 10 d. This can again point to a rotation period of 80 d where any time shift expresses itself at about one eighth of the rotation period (Collier Cameron et al. 2019; Mortier 2022). Perhaps more intriguingly, the data becomes mildly correlated after 50–70 d (depending on the direction of the time shift). This points

<sup>7</sup> <https://celerite.readthedocs.io/en/stable/>

<sup>8</sup> <https://github.com/hpparvi/PyDE>

to a rotational correlation timescale between  $H\alpha$  and RV of 120 d. While this is unlikely to be the rotational period considering the alternative measurements, it appears to be the timescale manifested in the data that we have. As seen later in Section 5, several values are identified for the GP rotational periodicity parameter when applying a wide GP prior, including 80 and 120 days. The mass of the planet is not affected by this.

#### 4 PHOTOMETRY MODELLING

We fit the available photometry from *TESS*, *CHEOPS*, and MuSCAT2/3 jointly in *juliet* (Espinoza et al. 2019). We use the six detrended *CHEOPS* visits that contain a transit of Gliese 12 b as well as the five *TESS* sectors, and four detrended MuSCAT2/3 observations across  $r$ ,  $i$ , and  $z$  bands. In order to detrend the *TESS* data, we include a GP with a Matérn-3/2 kernel (fitting for the amplitude of the GP, GP\_sigma, and the time-scale of the GP, GP\_rho). We fit for:

- the period,  $P$
- the time-of-transit centre,  $T_0$
- the planet-to-star radius ratio,  $R_{\text{pl}}/R_{\star}$
- the impact parameter,  $b$
- the stellar density,  $\rho$
- the limb darkening coefficients parametrised following Kipping (2013), for *TESS*, *CHEOPS*, and MuSCAT2/3  $r$ ,  $i$ , and  $z$  bands respectively
- the jitter, for *TESS*, *CHEOPS*, and MuSCAT2/3  $r$ ,  $i$ , and  $z$  bands respectively
- the offset relative flux, for *TESS*, *CHEOPS*, and MuSCAT2/3  $r$ ,  $i$ , and  $z$  bands respectively

Due to the isolated field, we fixed the dilution factor for *TESS*, *CHEOPS*, and MuSCAT2/3  $r$ ,  $i$ , and  $z$  bands to 1. We used the values for the period and time-of-transit centre derived from Kuzuhara et al. (2024) as priors in a normal distribution but inflated the width to be 0.1. We also set a normal distribution for the stellar density with the stellar values obtained from Kuzuhara et al. (2024). We let the other parameters vary uniformly. All the prior distributions are listed in Tables C1 and C2.

Finally, we performed two different fits, one assuming a circular orbit and one with free eccentricity and argument of periastron. Both fits resulted in higher precisions on the period and time-of-transit centre as compared to Dholakia et al. (2024) and Kuzuhara et al. (2024). Furthermore, the additional *TESS* sector and *CHEOPS* visit as well as the re-extraction of the *CHEOPS* data, and joint fitting with the MuSCAT2/3 photometry allows us to derive the planet radius from the fit more precisely. From the circular fit, we found a radius of  $0.963 \pm 0.034 R_{\oplus}$  while the eccentric solution gave a radius of  $0.904 \pm 0.035 R_{\oplus}$  with an eccentricity of  $0.39^{+0.17}_{-0.11}$ .

We adopt the eccentric fit as our final result. We show the phase-folded transits with the best-fit model from *juliet* in Figure 3. Final extracted values for the orbital and planetary parameters are listed in Table 5 and the stellar and instrumental parameters are listed in Table C3.

#### 5 RV MODELLING

We fitted the RVs (HARPS-N S-BART, ESPRESSO S-BART, and CARMENES SERVAL) using the *pyaneti* package<sup>9</sup>, presented by Barragán et al. (2019, 2022).

Within a periodogram of the RV data (see Figure B1), the signal of the planet is not apparent to any significance. However, since the orbital period and time-of-transit are known from photometric modelling, we used these results to inform the corresponding priors for this RV fit. Despite the small value of  $\log R'_{\text{HK}}$ , as shown in Table 3, there are also signs in the periodogram of possibly stellar-related signals in the data.

We use *pyaneti* as it is one of few packages that can model the RVs with a single GP, but it can also do multi-dimensional GP fitting, where multiple data sets are co-modelled with one common GP (Rajpaul et al. 2015; Barragán et al. 2022). We have used both functionalities when modelling the RVs, and also tried fitting without any GP at all. In all cases where a GP was used, we employ the quasi-periodic kernel and fit for the GP amplitudes ( $A_0$  for the single GP and adding in  $A_1$  and  $A_2$  for the multi-GP), the activity decay timescale ( $\lambda_e$ ), the inverse harmonic complexity ( $\lambda_p$ ), and the stellar rotation period ( $P_{\text{rot,GP}}$ ); see Rajpaul et al. (2015) and Barragán et al. (2022) for a more detailed description of the kernel.

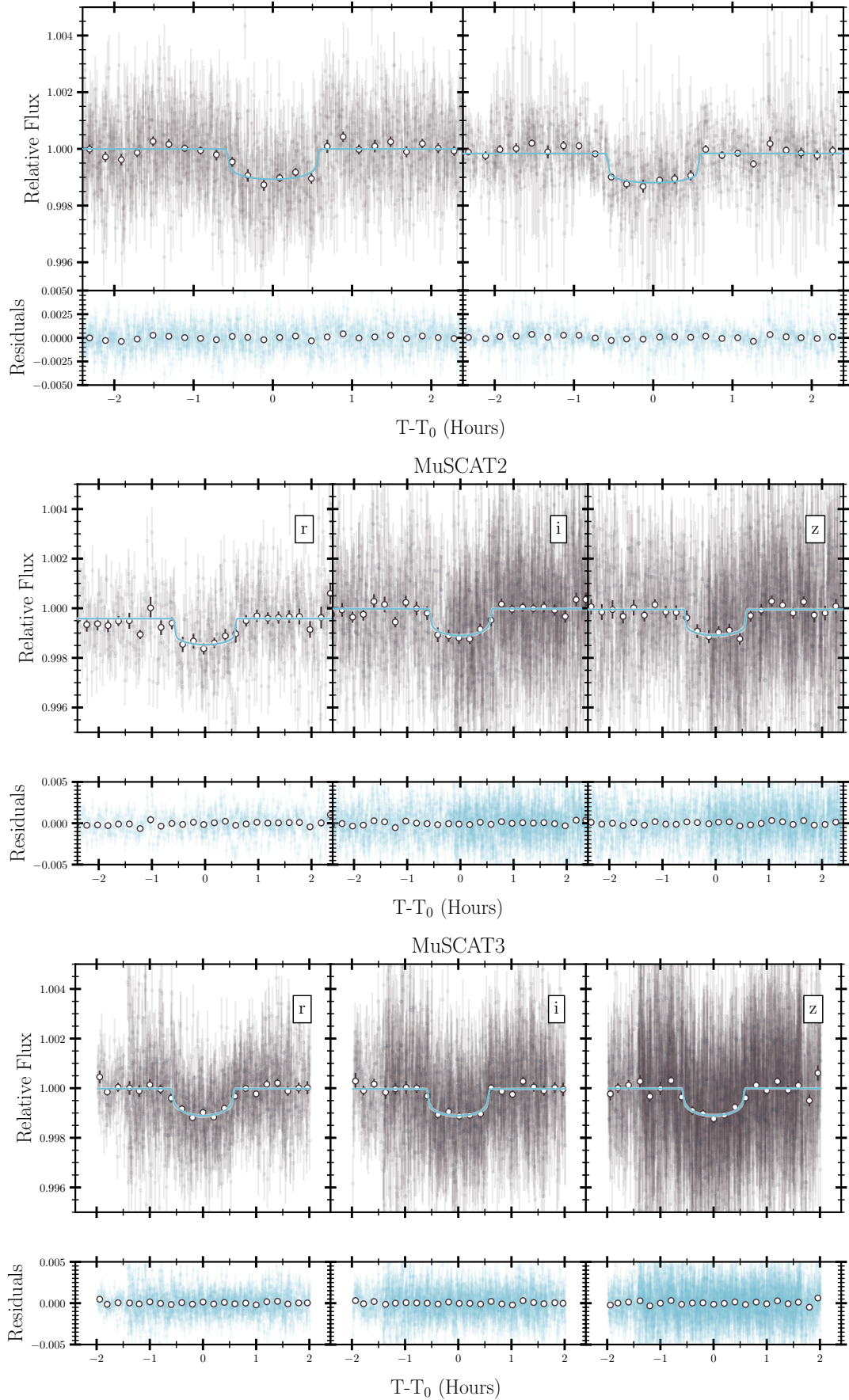
In all fits, the eccentricity,  $e$ , and argument of periastron,  $\omega$ , were reparameterised as  $\sqrt{e} \sin \omega$  and  $\sqrt{e} \cos \omega$ , as in Eastman et al. (2013). As aforementioned, the orbital period,  $P$ , and transit time,  $T_0$ , were fit with Gaussian priors, informed by the results of the photometry-only fit; the prior on  $T_0$  was adjusted (accounting for the uncertainty in  $P$ ) to ensure that it fell near the midpoint of the RV data. Finally, offsets and jitter corresponding to the individual instruments were also fitted as free parameters in the models. All prior distributions of the adopted fit can be found in Tables C1 and C2.

A multitude of runs were performed, including circular and eccentric models; no GP, single GP and multi-dimensional GPs. For the latter, various combinations of parameters (i.e., FWHM, BIS, and  $H\alpha$ ) were utilised in combination with the RVs. The rotation period prior was changed, allowing for a wide prior, a prior centred around 80 d motivated by the photometry, and a prior centred around 120 d motivated by the results of the wide prior and the coherence timescale between the RVs and the  $H\alpha$  indicator. All results constrain the planet parameters similarly and they are all consistent within less than  $0.5\sigma$ . Several results are virtually indistinguishable for the planet parameters, but the BIC values show preference for the model with a GP applied to the RVs with  $\Delta\text{BIC} = 77.9$  compared to the next-best model (no GP). We decided to adopt the results achieved from the model using a standard GP applied solely to the RV data, as the BIC values show preference for this model.

We measure an RV semi-amplitude of  $K = 0.70 \text{ m s}^{-1}$  with a  $3.6\sigma$  significance. The phase-folded model and data are presented in Figure 4. We thus find that Gliese 12 b has a mass of  $0.95^{+0.26}_{-0.27} M_{\oplus}$ , and an eccentricity of  $0.24^{+0.15}_{-0.12}$  constrained only at the  $2\sigma$  level. With the current dataset, we are not able to more-precisely constrain the eccentricity. Upon checking all the individual results, high consistency on the planet parameters was found between runs where parameters agreed well within 0.5 sigma. For some runs, this is shown in Figure 5.

It is recognised that the period of the GP does not always converge at the value of the rotational period that was identified via photometry (85 d). Additionally, constraining the GP period of around 85 d

<sup>9</sup> <https://github.com/oscaribv/pyaneti>

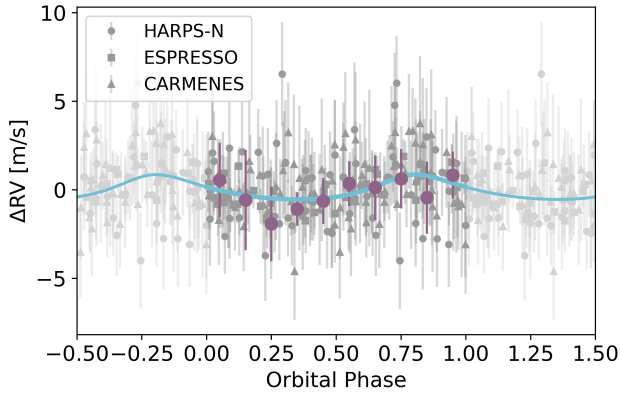


**Figure 3.** Detrended and phase-folded transits of Gliese 12 b with the best-fitted model from *juliet* plotted in blue as well as the residuals on the bottom. Top left: *TESS*; top right: *CHEOPS*, middle: *MuSCAT2*; bottom: *MuSCAT3*.

**Table 5.** Gliese 12 b orbital and planetary parameters for the three different fitting procedures. The fitted parameters are above the horizontal line and the derived parameters below. Exceptions are mentioned in the notes below the table.

Parameter	Unit	Photometry-only	Informed RV fit	Joint fit
$P$	(d)	$12.761417^{+0.000047}_{-0.000037}$	$12.761421 \pm 0.000047$	$12.761417^{+0.000060}_{-0.000054}$
$T_0$	(BJD)	$2459497.1855^{+0.0020}_{-0.0026}$	$2460492.5745^{+0.0045}_{-0.0043}$	$2460033.16353^{+0.00087}_{-0.00088}$
$R_p/R_\star$	—	$0.03080^{+0.00084}_{-0.00073}$	—	$0.0323^{+0.0015}_{-0.0015}$
$b$	—	$0.51^{+0.12}_{-0.12}$	—	$0.75^{+0.09}_{-0.17}$
$\rho_\star$	(g cm $^{-3}$ )	$19.211^{+1.183}_{-1.198}$	—	$19.008^{+1.549}_{-1.549}$
$K$	(m s $^{-1}$ )	—	$0.70^{+0.19}_{-0.20}$	$0.67^{+0.21}_{-0.22}$
$\sqrt{e} \sin \omega$	—	—	$-0.12^{+0.38}_{-0.33}$	$-0.08^{+0.42}_{-0.34}$
$\sqrt{e} \cos \omega$	—	—	$0.35^{+0.12}_{-0.20}$	$0.35^{+0.12}_{-0.24}$
$e$	—	$0.39^{+0.17}_{-0.11}$	$0.24^{+0.15}_{-0.12} (< 0.39)$	$0.25^{+0.13}_{-0.13} (< 0.38)$
$\omega$	(deg)	$143^{+28}_{-39}$	$-18^{+61}_{-41}$	$-15^{+69}_{-41}$
$a/R_\star$	—	$54.9^{+1.1}_{-1.2}$	—	$54.7^{+1.5}_{-1.6}$
$i$	(deg)	$89.47 \pm 0.13$	—	$89.236^{+0.069}_{-0.061}$
$M_p$	( $M_\oplus$ )	—	$0.95^{+0.26}_{-0.27}$	$0.91^{+0.28}_{-0.30}$
$R_p$	( $R_\oplus$ )	$0.904^{+0.037}_{-0.034}$	—	$0.92 \pm 0.05$
$\rho_p$	(g cm $^{-3}$ )	—	$7.0^{+2.3}_{-2.1}$	$6.4 \pm 2.4$

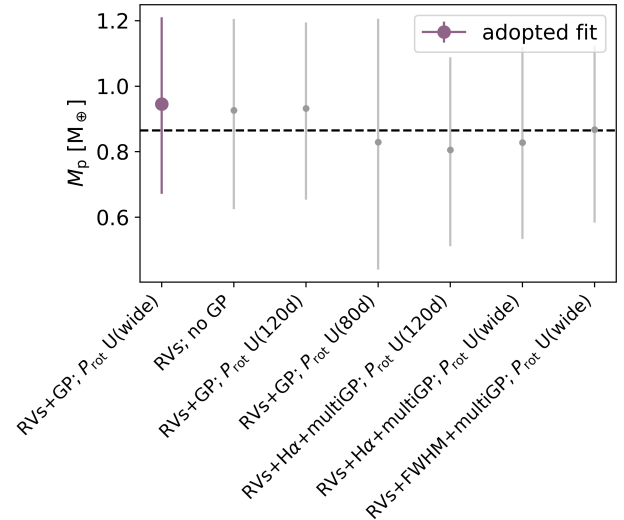
Notes: For the photometric fit,  $e$  and  $\omega$  are fitted directly; in the informed RV and the joint fit, they are derived. Numbers in brackets indicate the  $1\sigma$  upper limit for the value.

**Figure 4.** Phase-folded RVs from the best-fit informed RV model with GPs removed. Binned data shown by the large, purple points (10 bins). Phase-folded on the period of the planet (12.761421 d).

resulted in a poorer fit in comparison to a wider prior. Given that  $\langle \log R'_{\text{HK}} \rangle = -5.62$ , it is suspected that Gliese 12 is too quiet to confidently ascertain the rotational period using RV data alone. GP-free, multi-Keplerian fits were also run as discussed in Section 7.5.

## 6 JOINT PHOTOMETRY AND RV MODELLING

We used PyORBIT<sup>10</sup> (Malavolta et al. 2016, 2018) to perform a joint fit of the space-based transit observations, the RVs, and the spectroscopic activity index  $H\alpha$ . Transit modelling was performed

**Figure 5.** A summary of the variety of models fitted to the RV data. The purple point highlights the adopted fit. Here,  $\mathcal{U}(\text{wide})$  indicates wide uniform priors for the GP period (as in Table C2), and  $\mathcal{U}(\text{value})$  uniform indicates priors defined with 15 d either side of the specified value. The dashed, black line indicates the median mass value.

using PyTransit<sup>11</sup> (Parviainen 2015), while the red noise present in each light curve was modelled through the use of GPs, using a Matérn 3/2 kernel.

The RV systematics were also modelled with GPs, sharing certain hyperparameters with the  $H\alpha$  spectroscopic activity index to account

<sup>10</sup> Available at <https://github.com/LucaMalavolta/PyORBIT>

<sup>11</sup> <https://github.com/hpparvi/PyTransit>

for stellar activity. We adopted a quasi-periodic with cosine (QPC) kernel (Perger et al. 2021), with the stellar rotation period ( $P_{\text{rot}}$ ), the decay timescale of active regions ( $\lambda$ ), and the coherence scale ( $w$ ) as common (and free) hyperparameters for both the RV and H $\alpha$  time series. Although we have an estimate of stellar rotation based on long-term photometric observations, we imposed a uniform prior on  $P_{\text{rot}}$  in the range [60 d, 200 d] to see if we could recover the estimated photometric value of stellar rotation.

To speed up the analysis, we limited the *TESS* data to 12-hour time windows centred on the predicted mid-transit times. For both the *TESS* and *CHEOPS* transit light curves, the following parameters were fitted: the central time of transit ( $T_0$ ), the orbital period ( $P$ ), eccentricity ( $e$ ), and argument of periastron ( $\omega$ ), using the parameterisation from Eastman et al. (2013) ( $\sqrt{e} \sin \omega$ ,  $\sqrt{e} \cos \omega$ ). We also fitted the quadratic limb-darkening coefficients ( $u_1$ ,  $u_2$ ), constrained by normal priors based on predicted values from LDTR<sup>12</sup> (Husser et al. 2013; Parviainen & Aigrain 2015), as well as the impact parameter ( $b$ ) and the planet-to-star radius ratio ( $R_p/R_*$ ). We also fitted the stellar density ( $\rho_*$ ) using a normal prior based on the stellar parameters presented in (Kuzuhara et al. 2024). Each light curve included a white noise term as an additional free parameter.

For the RV data, we subtracted the median velocities from the HARPS-N and ESPRESSO datasets to place them on a similar scale to the CARMENES data, which is centred near 0 m s<sup>-1</sup>. The subtracted values correspond to median velocities of  $\gamma_{\text{HN}} = 51337.25$  m s<sup>-1</sup> and  $\gamma_{\text{ESP}} = 51409.56$  m s<sup>-1</sup>, respectively. Since we included instrument-specific offsets and jitter terms as free parameters in our model, these offsets have no effect on the RV fit. In addition to these offsets, we also fitted for the orbital period, eccentricity, and RV semi-amplitude ( $K$ ). As noted above, some GP hyperparameters were shared between the RV and H $\alpha$  time series. The kernel amplitude ( $H$ ) and the amplitude of the cosine component ( $C$ ) were fitted independently for each time series, while  $P_{\text{rot}}$ ,  $\lambda$ , and  $w$  were shared and fitted jointly.

The joint fit was performed in two stages. First, we applied global optimisation of the parameters using PyDE. Starting from the optimal solution, the parameter space was subsequently explored using emcee, running for  $2 \times 10^6$  iterations to meet the convergence criteria of PyORBIT. The final fitted orbital and planetary parameters and corresponding priors are listed in Tables 5 and C1, respectively. Similarly, the stellar and instrumental priors and resulting values are listed in Tables C2 and C3.

Our joint fit yields results for Gliese 12 b that are consistent with those obtained from the photometry-only and informed RV analyses. The simultaneous modelling of the RVs and the H $\alpha$  activity index using the QPC kernel produced a rotation period of  $P_{\text{rot}} = 171.9^{+1.6}_{-1.7}$  d. This value is close to twice the rotation period inferred from long-term photometry ( $P_{\text{rot}} \sim 85$  d). Since the QPC kernel models both  $P_{\text{rot}}$  and  $P_{\text{rot}}/2$  (see Perger et al. 2021), the likely stellar rotation period of 85 d is still accounted for by the kernel. Tests using the QPC kernel on the RV and H $\alpha$  datasets separately showed that the kernel can recover the 85-day rotation period when a uniform prior in the range [60 d, 100 d] is used for  $P_{\text{rot}}$ . A stellar rotation period longer than 100 d appears unlikely, as M stars with such long periods are rare (see Newton et al. 2016; Shan et al. 2024). Therefore, a rotation period close to 85 d remains the more plausible scenario for Gliese 12.

## 7 DISCUSSION

All the orbital and planetary parameters are consistent across the different fits. For the upcoming discussion of Gliese 12 b, we adopt as final parameters the values from the individual photometry fit and the RV fit informed by that fit (Sections 4 and 5).

### 7.1 Gliese 12 b as an exo-Venus

Gliese 12 b occupies a unique region of parameter space due to its distinctive physical properties. For comparison reasons, we use the well-curated PlanetS database (Parc et al. 2024) maintained on the DACE platform<sup>13</sup>. We further limit it to all planets with a radius lower than  $2 R_{\oplus}$ . Figure 6 shows the mass–radius diagram of this sample of small planets. It is directly obvious that Gliese 12 b lies in the same part of parameter space as Earth and Venus with a radius closer to Venus. Its density makes it marginally denser than our rocky Solar System planets.

The orbital period of Gliese 12 b is much smaller than those of Earth and Venus. However, since the host star is an M dwarf, Gliese 12 b is actually a temperate planet too. We have calculated its equilibrium temperature following Cowan & Agol (2011). As the albedo is unknown, we have to make an assumption. We calculated the equilibrium temperature three times, using an albedo of 0, as well as both Earth’s and Venus’ albedo (0.31 and 0.77 respectively). We found that the equilibrium temperature of Gliese 12 b is between 315 and 218 K. When using Venus’ albedo, the equilibrium temperature of Gliese 12 b is extremely close to that of Venus itself. Combined with the more Venus-like radius, we could conclude that this planet is possibly Venus-like.

Figure 7 shows the different positions of Gliese 12 b in a planet density versus equilibrium temperature diagram. We caveat that different albedo’s may have been used for the PlanetS database. In any case, whichever the true equilibrium temperature, Gliese 12 b occupies a sparsely populated area in this parameter space, making it a truly remarkable characterised exoplanet. The only other well-characterised temperate Earth-size, Earth-mass planets are LHS1140 b (Cadioux et al. 2024) characterised by ESPRESSO, and the TRAPPIST-1 planets (Agol et al. 2021) where mass measurements come from transit timing variations.

As its host star is also one of the closest known planet host stars, there are plenty of opportunities for continued follow up of this exo-Venus. Additional information on atmospheric properties, and further and deeper characterisation of the system will reveal how similar (or discrepant) Gliese 12 b is from Venus itself.

### 7.2 Interior composition modelling

Having a planetary mass and radius for Gliese 12 b, we calculate a mean bulk density of  $7.0^{+2.3}_{-2.1}$  g cm<sup>-3</sup>, suggesting it is ever so slightly denser than Earth and Venus. We can also model the possible interior compositions for this small planet. For this purpose, we use the publicly available interior modelling code pLaNETic<sup>14</sup> (Egger et al. 2024). This framework utilises a neural network that was trained on the BICEPS forward model (Haldemann et al. 2024). This was combined with a full grid accept-reject sampling scheme. pLaNETic has been shown to be fast as well as reliable when characterising the possible interior compositions of small planets.

<sup>12</sup> <https://github.com/hpparvi/ldtk>

<sup>13</sup> <https://dace.unige.ch/exoplanets/>

<sup>14</sup> <https://github.com/joannegger/plaNETic>

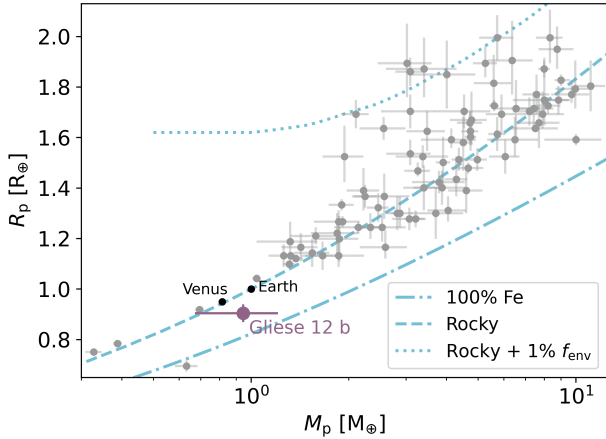


**Figure 6.** Mass-radius diagram of all small planets ( $R_p \leq 2 R_\oplus$ ) in the PlanetS database (grey), Earth and Venus (black), and Gliese 12 b (large purple). The 100 per cent Fe and rocky compositional lines are taken from Zeng et al. (2019), and the rocky + 1 per cent  $f_{\text{env}}$  line is from Chen & Rogers (2016).

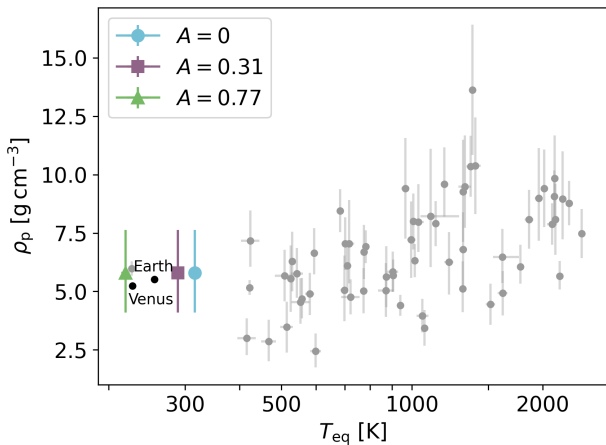


**Figure 7.** Planetary density versus equilibrium temperature for the same sample of planets as in Figure 6. For Gliese 12 b, different Bond albedo values were used:  $A = 0$ , Earth’s albedo ( $A = 0.31$ ), and Venus’ albedo ( $A = 0.77$ ).

Within `planETic`, a planet can have up to three layers: an inner core made of iron (Fe) and sulphur (S), a rocky mantle composed of oxidised silicon (Si), magnesium (Mg) and Fe, and a volatile layer uniformly mixed between water and pure hydrogen-helium. It thus does not have a separate water layer. We assume in the model that the planet formed outside the ice line and all water was thus accreted in the form of ice (see Egger et al. 2024, for more detail). Considering the current equilibrium temperature of Gliese 12b and assuming some form of migration during planet formation and evolution, this is a reasonable assumption to make.

Different compositional priors can further be set based on the host star. There are preliminary studies showing possible links between host star and planet composition (e.g. Thiabaud et al. 2015; Mortier et al. 2020; Adibekyan et al. 2021). However, the exact link is still unknown which is why `planETic` allows for the different priors. The

relevant priors relate to the Si/Mg/Fe ratios. They can be sampled uniformly, they can have a prior where the planet ratios are assumed to be equal to the star’s (Thiabaud et al. 2015), and they can have a prior assuming the planet is iron-enriched compared to the star (Adibekyan et al. 2021).

The resulting mass fractions of the different layers are shown in Figure 8. As expected for this planet, the volatile mass fraction is small and consistent with 0. The core mass fraction is loosely constrained with median values between 20 and 30 per cent, depending on the prior. This is in line with the known core mass fraction of Venus (32 per cent).

### 7.3 Atmospheric mass loss

Gliese 12 b is also an intriguing target for transmission spectroscopy in the Lyman- $\alpha$  line. Lyman- $\alpha$  observations can reveal escaping hydrogen gas during exoplanet transits (Vidal-Madjar et al. 2003), but interstellar absorption and geocoronal emission often obscure the line core, leaving observations to be sensitive only in the high-velocity line wings (e.g. Ehrenreich et al. 2015). Nearby systems with high systemic RVs offer both higher flux and weaker interstellar absorption and will offset the interstellar absorption line core from the stellar emission line core. This allows to reveal information content at lower velocities and these targets are thus ideal for these studies. regg At a distance of 12.2 pc and a systemic velocity of  $51.2 \text{ km s}^{-1}$ , the Gliese 12 system satisfies both of these criteria. Using the serendipitous detection of X-ray emission from Gliese 12 by *XMM-Newton* ( $F_X = 6.8 \pm 2.4 \times 10^{-15} \text{ erg cm}^{-2} \text{ s}^{-1}$ ; Webb et al. 2020) and the Linsky et al. (2013) relation between Lyman- $\alpha$  and X-ray flux, we expect Gliese 12 to have an intrinsic Lyman- $\alpha$  flux of  $1.1 \times 10^{-13} \text{ erg cm}^{-2} \text{ s}^{-1}$ . Based on the modest column density of neutral hydrogen predicted by the Colorado LISM model (Redfield & Linsky 2000) of  $N_H = 1.1 \times 10^{18} \text{ cm}^{-2}$  and the high systemic RV, we expect Gliese 12 b to be a suitable target for Lyman- $\alpha$  transmission spectroscopy. It will soon be observed for this purpose by *HST* GO 17600 (PI: Vissapragada).

We additionally simulated the past evaporation history of Gliese 12 b in order to determine whether a H/He-rich envelope would have survived to the present day under X-ray irradiation from its host star.

We adopted the method by Fernández Fernández et al. (2023), which combines three components to simulate the evaporation history of close-in exoplanets; these are (1) a model of the X-ray emission history of the host star, (2) an envelope structure model that links the mass fraction of the H/He atmosphere to its thickness, and (3) a model for the atmospheric escape rate.

Regarding the X-ray emission history model, in Figure 9 we compared the *XMM-Newton* detection of Gliese 12 with the X-ray luminosity–age relations by Johnstone et al. (2021), which is based on a rotational evolution model fitted to open clusters, and by Engle (2024), which is based on empirical fits to populations of M-dwarfs. We found the model by Engle (2024) is much more consistent with the *XMM-Newton* measurement, within a factor of x5, and thus we favoured it over the model by Johnstone et al. (2021), which is x12 brighter. We additionally considered an alternative X-ray emission history for Gliese 12 where we scaled down the model by Engle (2024) to fit the *XMM-Newton* measurements.

Regarding the envelope structure model, we adopted the model by Chen & Rogers (2016), based on MESA simulations of planetary atmospheres. As for the mass loss model, we adopted the prescription by Kubyskhina et al. (2018), which accounts for both core-powered mass loss as well as energy-limited and recombination-limited X-ray-driven escape, and is based on hydrodynamic simulations.

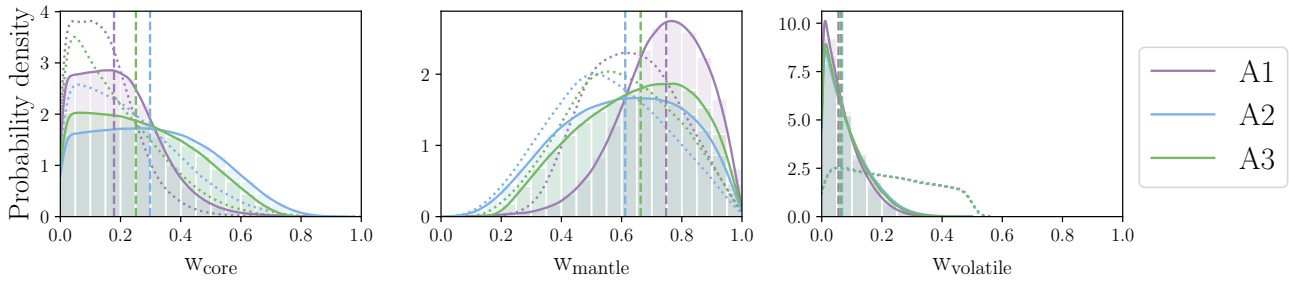


**Figure 8.** Posterior distributions (solid lines) of the interior structure of Gliese 12 b, showing, from left to right, the mass fractions of the inner core, mantle, and volatile components. The different colours represent the three different priors for the planetary Si/Mg/Fe ratios: stellar (purple, A1), iron-enriched (blue, A2), and uniform (green, A3). Dotted lines indicate the priors and vertical dashed lines show the median of each posterior distribution.

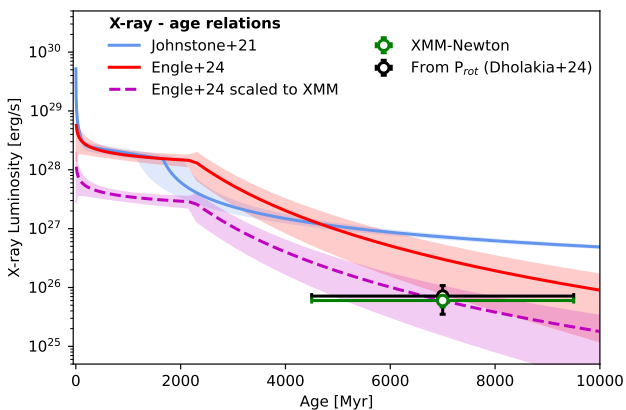


**Figure 9.** Comparison of several X-ray luminosity - age relations with the *XMM-Newton* observation of Gliese 12 (green circle). The plotted X-ray age relations are: [Johnstone et al. \(2021\)](#), [Engle \(2024\)](#), and the same model scaled down to fit the *XMM-Newton* measurement. The X-ray luminosity determined from the spin period measured by [Dholakia et al. \(2024\)](#) and the rotation-activity relation by [Engle & Guinan \(2023\)](#) is also shown (black circle) and is in very good agreement with the measured X-ray emission.

Motivated by its high density, we assumed that Gliese 12 b has no gaseous envelope at present. We then considered a number of initial envelopes on the planet, with mass fractions of 1 per cent, 2 per cent, and 5 per cent. We do not consider larger initial atmospheres as these would have been stripped off and truncated by boil-off processes shortly after dispersal of the protoplanetary disc ([Rogers et al. 2024](#)).

We thus simulated the past evaporation history of Gliese 12 b in each scenario using the photoevolver code ([Fernández Fernández et al. 2023](#)). We adopted the 4th-order Runge-Kutta integration method with a maximum time step of 1 Myr, starting from the age of 10 Myr to 1 Gyr.

In Figure 10 we show the results from our simulations. On the top panel we show atmospheric evolution under the X-ray emission history predicted by [Engle \(2024\)](#), and on the bottom panel, under the same emission history, but scaled down by a factor of 5 to match the *XMM-Newton* observation of Gliese 12 as we don't know the true X-ray history of the star. We found that all H/He envelopes are fully stripped from Gliese 12 b within 100 Myr, with none surviving to the

present day. Even with the fainter X-irradiation model, its lifetime is only extended to the age of 200 Myr.

#### 7.4 Prospects for atmospheric characterization

Given its high mean density and the intense XUV irradiation from its host star, Gliese 12 b is unlikely to have retained a primordial or secondary atmosphere rich in H<sub>2</sub>/He (see Section 7.3). Nonetheless, owing to the brightness of its host star, Gliese 12 b stands as one of the top rocky targets for atmospheric follow-up with JWST. Following [Kempton et al. \(2018\)](#), the planet has a Transmission Spectroscopy Metric (TSM) of  $13_{-3}^{+5}$ , similar to that of the TRAPPIST-1 planets.

We conducted simulations of transmission and emission spectra for realistic atmospheric scenarios, as they would be observed with various JWST instrument configurations (Figure 11). In particular, we modeled a Venus-like atmosphere consisting of 100 per cent CO<sub>2</sub>, motivated by the planet's physical parameters resembling those of Venus (see Section 7.1); a steam H<sub>2</sub>O envelope representing a water-world scenario; and a lighter steam CH<sub>4</sub> envelope featuring a reduced environment. We used TauREx 3 for radiative transfer modeling ([Waldmann et al. 2015a,b](#); [Al-Refaie et al. 2021](#)), employing a temperature-pressure profile similar to that of Venus for the CO<sub>2</sub> atmosphere and profiles adapted from [Kempton et al. \(2023\)](#) for the H<sub>2</sub>O and CH<sub>4</sub> compositions. The corresponding JWST spectra were generated using ExoTETHyS ([Morello et al. 2021](#)) for the NIRSpec G140H (0.97–1.83 μm), G235H (1.66–3.07 μm), and G395H (2.88–5.18 μm) modes, as well as the MIRI LRS Slitless (5–10 μm) mode, based on updated instrument response files and including an additional 30 per cent noise contribution in the final error bars. The popular NIRISS SOSS mode was excluded due to detector saturation after the first group. We adopted spectroscopic binning with a resolving power of  $R \sim 100$  for the NIRSpec modes, following the recommendations of [Carter et al. \(2024\)](#) and [Davey et al. \(2025\)](#), and a constant bin size of 0.25 μm for the MIRI LRS, as suggested by [Powell et al. \(2024\)](#). The predicted error bars for a single transit observation are 32–56 ppm (mean error 38 ppm) for NIRSpec G140H, 33–54 ppm (mean error 40 ppm) for NIRSpec G235H, 37–70 ppm (mean error 47 ppm) for NIRSpec G395H, and 41–63 ppm (mean error 49 ppm) for MIRI LRS. These uncertainties are comparable to or smaller than the expected spectral features in transmission, which reach  $\lesssim 50$  ppm in the most favorable CH<sub>4</sub>-dominated scenario. The emission spectra are generally flat across the wavelength range covered by our instrumental simulations, except for an  $\sim 80$  ppm CO<sub>2</sub> feature in the Venus-like scenario. Another possibility is to measure

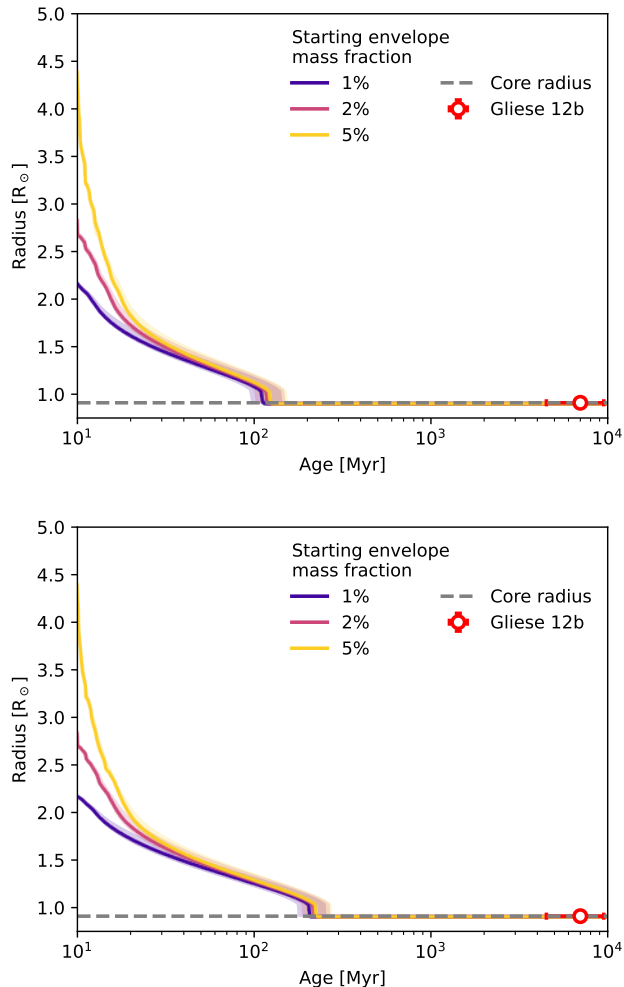


**Figure 10.** **Top panel:** evolution of the radius of Gliese 12 b under atmospheric escape using the X-ray irradiation history predicted by Engle (2024), with a range of initial atmospheres with mass fractions of 1 per cent (blue line), 2 per cent (red line), and 5 per cent (yellow line). The present-day radius and age of Gliese 12 b is plotted as a red circle, and its radius as a dashed grey line. **Bottom panel:** evolution of the radius of Gliese 12 b under atmospheric escape, following the top panel, using the X-ray irradiation history predicted by Engle (2024) scaled down by a factor of 5 to match the *XMM-Newton* observation.

planetary emission at longer wavelengths. In fact, Gliese 12 b is a target under consideration for the Rocky World DDT program (Redfield et al. 2024), potentially aiming to observe multiple secondary eclipses using a MIRI filter centered at  $15 \mu\text{m}$ . In all cases, multiple visits are required to robustly detect atmospheric features, with the optimal strategy, transmission or emission spectroscopy, depending on the actual atmospheric composition of Gliese 12 b.

### 7.5 Possibility of extra planets in the system

The possibility of there being more planets within the system still remains, and further investigation is needed to reveal any previously-undetected signals. We have performed additional RV fits using two eccentric Keplerian models to explore any potential multi-planet configurations of small planets with periods below 50 days (based

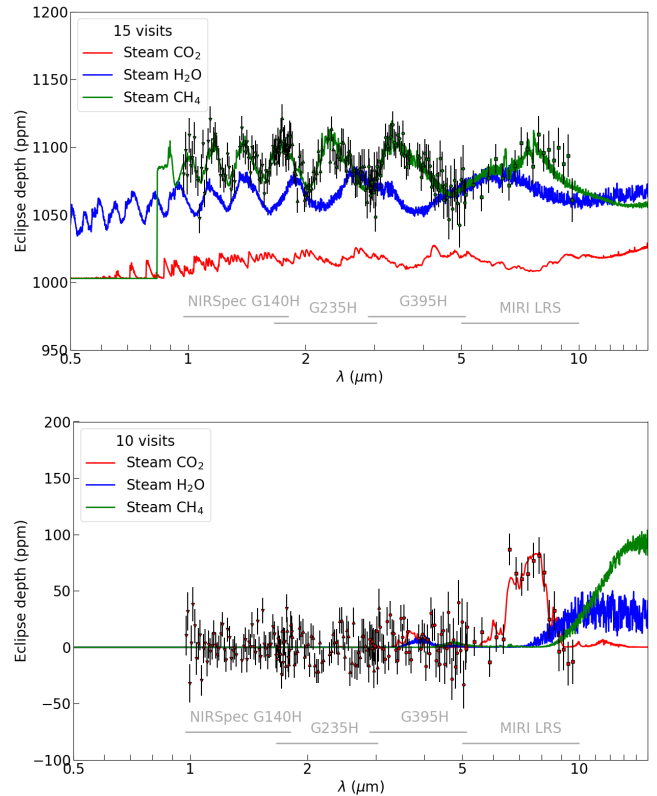


**Figure 11.** **Top panel:** Modelled transmission spectra of Gliese 12 b, assuming an atmospheric composition of 100 per cent  $\text{CO}_2$  (red), 100 per cent  $\text{H}_2\text{O}$  (blue), and 100 per cent  $\text{CH}_4$  (green). Points with error-bars show the simulated spectrum for the  $\text{CH}_4$  composition, combining 15 transits with each of the NIRSpec G140H, G235H, G395H and MIRI LRS Slitless modes. **Bottom panel:** Analogous emission spectra. Points with error-bars show the simulated spectrum for the  $\text{CO}_2$  composition, combining 10 eclipses with each of the NIRSpec G140H, G235H, G395H and MIRI LRS Slitless modes.

of the periodogram information). While a solution was found with a second Keplerian close to 34 days, the parameters were poorly constrained and the single-Keplerian model with a GP applied to the RVs was preferred using the BIC. We obtain  $\text{BIC} = -1774.7$  versus  $\text{BIC} = -1846.5$  for the two-Keplerian model and the adopted model, respectively.

Ultimately, more data are required to constrain any existing secondary signals, and authenticate the system architecture. More RV data will further allow for the resolution of current degeneracies that exist between eccentricity, stellar activity, and any undetected planetary companions and make the mass measurement of Gliese 12 b more robust. Obtaining more RVs with the precision of those within this study could reveal planets hidden below the current precision floor of the dataset.

## 8 CONCLUSIONS

In this paper, we present new analyses of the transiting exo-Venus, Gliese 12 b. We performed a photometry-only fit, an informed RV fit, and a joint fit using both datasets simultaneously.

With new *TESS* and *CHEOPS* observations, we report refined period ( $12.76 \text{ d}$ ) and radius measurements ( $0.904^{+0.037}_{-0.034} R_{\oplus}$ ), yielding

at least a 40 per cent improvement in radius precision when compared to previous studies (Dholakia et al. 2024; Kuzuhara et al. 2024).

Using nearly 200 high-precision RV observations from HARPS-N, ESPRESSO, and CARMENES, we report the first definitive mass measurement of Gliese 12 b. Owing to the extremely small RV semi-amplitude of Gliese 12 b, we adopted a variety of modelling approaches dealing with the stellar signals in different ways. We detect an RV semi-amplitude of  $0.70^{+0.19}_{-0.20} \text{ m s}^{-1}$  ( $3.6\sigma$ ), yielding a mass measurement of  $0.95^{+0.26}_{-0.27} M_{\oplus}$ . This measurement is among the smallest semi-amplitudes ever measured for a transiting planet and is pushing the boundaries of our current capabilities.

A thorough investigation was conducted into the activity signal of Gliese 12. Analysis of long-term photometric monitoring from ASAS-SN, LCOGT, TJO, and E-EYE – as well as a DCF analysis of the RV and  $H\alpha$  data – provided further evidence towards a rotation period of approximately 85 d (see Figure A1). This work highlights the importance of the rigorous treatment of stellar variability when searching for the smallest exoplanets in RV data.

Gliese 12 b stands out with its physical and orbital properties. We investigated the nature of Gliese 12 b, by studying its interior structure, atmospheric mass loss history and future atmospheric prospects. Interior structure modelling revealed that Gliese 12 b is likely to be similar to Venus in composition (predominantly rocky make-up). The bulk properties of this planet place it in a unique region of parameter space, distinguishing it from other exoplanets with similar properties (see Figures 6 and 7). Furthermore, we demonstrated that the planet is unlikely to have retained a primordial gaseous envelope, given the X-ray emission history of its host star. Given its intriguing properties, Gliese 12 b presents a promising opportunity for Lyman- $\alpha$  spectroscopic follow-up studies, and is already being observed with *HST* for this reason. It is also a fantastic target for the Rocky Worlds DDT programme on *JWST*.

## ACKNOWLEDGEMENTS

This work is based on observations made with the Italian Telescopio Nazionale Galileo (TNG) operated on the island of La Palma by the Fundación Galileo Galilei of the INAF (Istituto Nazionale di Astrofisica) at the Spanish Observatorio del Roque de los Muchachos of the Instituto de Astrofísica de Canarias. The HARPS-N project was funded by the Prodex Program of the Swiss Space Office (SSO), the Harvard University Origin of Life Initiative (HUOLI), the Scottish Universities Physics Alliance (SUPA), the University of Geneva, the Smithsonian Astrophysical Observatory (SAO), the Italian National Astrophysical Institute (INAF), University of St. Andrews, Queen’s University Belfast, and University of Edinburgh.

CARMENES is an instrument at the Centro Astronómico Hispano en Andalucía (CAHA) at Calar Alto (Almería, Spain), operated jointly by the Junta de Andalucía and the Instituto de Astrofísica de Andalucía (CSIC). CARMENES was funded by the Max-Planck-Gesellschaft (MPG), the Consejo Superior de Investigaciones Científicas (CSIC), the Ministerio de Economía y Competitividad (MINECO) and the European Regional Development Fund (ERDF) through projects FICTS-2011-02, ICTS-2017-07-CAHA-4, and CAHA16-CE-3978, and the members of the CARMENES Consortium (Max-Planck-Institut für Astronomie, Instituto de Astrofísica de Andalucía, Landessternwarte Königstuhl, Institut de Ciències de l’Espai, Institut für Astrophysik Göttingen, Universidad Complutense de Madrid, Thüringer Landessternwarte Tautenburg, Instituto de Astrofísica de Canarias, Hamburger Sternwarte, Centro de Astrobiología and Centro Astronómico Hispano-Alemán), with

additional contributions by the MINECO, the Deutsche Forschungsgemeinschaft (DFG) through the Major Research Instrumentation Programme and Research Unit FOR2544 “Blue Planets around Red Stars”, the Klaus Tschira Stiftung, the states of Baden-Württemberg and Niedersachsen, and by the Junta de Andalucía.

This work is based on observations collected with ESPRESSO at the European Southern Observatory under ESO programme 113.26RH.

*CHEOPS* is an ESA mission in partnership with Switzerland with important contributions to the payload and the ground segment from Austria, Belgium, France, Germany, Hungary, Italy, Portugal, Spain, Sweden, and the United Kingdom. The *CHEOPS* Consortium would like to gratefully acknowledge the support received by all the agencies, offices, universities, and industries involved. Their flexibility and willingness to explore new approaches were essential to the success of this mission. *CHEOPS* data analysed in this article will be made available in the *CHEOPS* mission archive ([https://cheops.unige.ch/archive\\_browser/](https://cheops.unige.ch/archive_browser/)).

This paper made use of data collected by the TESS mission and are publicly available from the Mikulski Archive for Space Telescopes (MAST) operated by the Space Telescope Science Institute (STScI). Funding for the TESS mission is provided by NASA’s Science Mission Directorate. We acknowledge the use of public TESS data from pipelines at the TESS Science Office and at the TESS Science Processing Operations Center. Resources supporting this work were provided by the NASA High-End Computing (HEC) Program through the NASA Advanced Supercomputing (NAS) Division at Ames Research Center for the production of the SPOC data products. This research has made use of the Exoplanet Follow-up Observation Programme (ExoFOP; DOI: 10.26134/ExoFOP5) website, which is operated by the California Institute of Technology, under contract with the National Aeronautics and Space Administration under the Exoplanet Exploration Programme.

This work has made use of data from the European Space Agency (ESA) mission *Gaia* (<https://www.cosmos.esa.int/gaia>), processed by the *Gaia* Data Processing and Analysis Consortium (DPAC, <https://www.cosmos.esa.int/web/gaia/dpac/consortium>). Funding for the DPAC has been provided by the Instituto de Astrofísica e Ciências do Espaço, CAUP, Universidade do Porto, Rua das Estrelas, 4150-762 Porto, Portugal

<sup>35</sup>Departamento de Física e Astronomia, Faculdade de Ciências, Universidade do Porto, Rua do Campo Alegre, 4169-007 Porto, Portugal

<sup>36</sup>Space sciences, Technologies and Astrophysics Research (STAR) Institute, Université de Liège, Allée du 6 Août 19C, 4000 Liège, Belgium

<sup>37</sup>Astrobiology Research Unit, Université de Liège, Allée du 6 Août 19C, B-4000 Liège, Belgium

provided by national institutions, in particular the institutions participating in the *Gaia* Multilateral Agreement.

This publication makes use of The Data & Analysis Center for Exoplanets (DACE), which is a facility based at the University of Geneva (CH) dedicated to extrasolar planets data visualisation, exchange and analysis. DACE is a platform of the Swiss National Centre of Competence in Research (NCCR) PlanetS, federating the Swiss expertise in Exoplanet research. The DACE platform is available at <https://dace.unige.ch>.

This research has made use of the NASA Exoplanet Archive, which is operated by the California Institute of Technology, under contract with the National Aeronautics and Space Administration under the Exoplanet Exploration Program.

DAT acknowledges the support of the Science and Technology Facilities Council (STFC).

YNEE acknowledges support from a Science and Technology Facilities Council (STFC) studentship, grant number ST/Y509693/1.

AM, AAJ, BSL acknowledge funding from a UKRI Future Leader Fellowship, grant number MR/X033244/1. AM acknowledges funding from a UK Science and Technology Facilities Council (STFC) small grant ST/Y002334/1.

TGW acknowledges support from the University of Warwick and UKSA.

We acknowledge financial support from the Agencia Estatal de Investigación of the Ministerio de Ciencia e Innovación MCIN/AEI/10.13039/501100011033 and the ERDF “A way of making Europe” through projects PID2021-125627OB-C3[1:2], PID2023-152906NA-I00, and PID2022-137241NBC4[1:4], PID2019-107061GB-C61, CNS2023-144309 and PID2020-112949GB-I00 and from the Centre of Excellence “Severo Ochoa” award to the Instituto de Astrofísica de Canarias (CEX2021-001131-S).

This research was partially funded by The Israel Science Foundation through grant No. 1404/22.

This work was funded by the European Union (ERC, FIERCE, 101052347). Views and opinions expressed are however those of the author(s) only and do not necessarily reflect those of the European Union or the European Research Council. Neither the European Union nor the granting authority can be held responsible for them. This work was also supported by FCT - Fundação para a Ciência e a Tecnologia through national funds by these grants: UIDB/04434/2020 DOI: 10.54499/UIDB/04434/2020, UIDP/04434/2020 DOI: 10.54499/UIDP/04434/2020, PTDC/FIS-AST/4862/2020, UID/04434/2025. CEECIND/CP2839/CT0004, 2023.08117.CEECIND/CP2839/CT0004.

SD acknowledges support from the Deutsche Forschungsgemeinschaft under Research Unit FOR2544 “Blue Planets around Red Stars”, project no. DR 281/39-1.

APH acknowledges the support from the Deutsche Forschungsgemeinschaft (DFG) under Research Unit FOR 2544 “Blue Planets around Red Stars” through project HA 3279/14-1.

LN and LM acknowledge financial contribution from the INAF Large Grant 2023 “EXODEMO”.

AVF acknowledges the support of the Institute of Physics through the Bell Burnell Graduate Scholarship Fund.

LM acknowledges the financial contribution from PRIN MUR 2022 project 2022J4H55R.

ASB acknowledges financial contribution from the European Union - Next Generation EU RRF M4C2 1.1 PRIN MUR 2022 project 2022CERJ49 (ESPLORA).

TT acknowledges support from the BNSF program “VIHREN-2021” project No. KP-06-DV/5.

IC acknowledges financial contribution from the European Union - Next Generation EU PNRR M4C2 1.2 project SOE2024.

MS thanks the Belgian Federal Science Policy Office (BELSPO) for the provision of financial support in the framework of the PRODEX Programme of the European Space Agency (ESA) under contract number C4000140754.

This work has been carried out within the framework of the NCCR PlanetS supported by the Swiss National Science Foundation under grants 51NF40\_182901 and 51NF40\_205606.

ACC acknowledges support from STFC consolidated grant number ST/V000861/1 and UKRI/ERC Synergy Grant EP/Z000181/1 (REVEAL).

EN acknowledges the support from the Deutsches Zentrum für Luft- und Raumfahrt (DLR, German Aerospace Center) - project number 50OP2502.

## DATA AVAILABILITY

The photometric data is publicly available via the respective archives. The RVs will be released via Vizier CDS.

## REFERENCES

- Adibekyan V., et al., 2021, *Science*, **374**, 330
- Agol E., et al., 2021, *The Planetary Science Journal*, **2**, 1
- Al-Refaie A. F., Changeat Q., Waldmann I. P., Tinetti G., 2021, *ApJ*, **917**, 37
- Astudillo-Defru N., Delfosse X., Bonfils X., Forveille T., Lovis C., Rameau J., 2017, *A&A*, **600**, A13
- Baglin A., 2003, *Advances in Space Research*, **31**, 345
- Bailer-Jones C. A. L., Rybizki J., Fouesneau M., Demleitner M., Andrae R., 2021, *AJ*, **161**, 147
- Barragán O., Gandolfi D., Antoniciello G., 2019, *MNRAS*, **482**, 1017
- Barragán O., Aigrain S., Rajpaul V. M., Zicher N., 2022, *MNRAS*, **509**, 866
- Basant R., et al., 2025, *ApJ*, **982**, L1
- Bauer F. F., Zechmeister M., Reiners A., 2015, *A&A*, **581**, A117
- Benz W., et al., 2021, *Experimental Astronomy*, **51**, 109
- Bonomo A. S., et al., 2023, *A&A*, **677**, A33
- Borucki W. J., et al., 2010, *Science*, **327**, 977
- Brandeker A., Patel J. A., Morris B. M., 2024, PIPE: Extracting PSF photometry from CHEOPS data, Astrophysics Source Code Library, record ascl:2404.002
- Brown T. M., et al., 2013, *PASP*, **125**, 1031
- Caballero J. A., et al., 2016, in Peck A. B., Seaman R. L., Benn C. R., eds, Society of Photo-Optical Instrumentation Engineers (SPIE) Conference Series Vol. 9910, Observatory Operations: Strategies, Processes, and Systems VI. p. 99100E, doi:10.1117/12.2233574
- Cadieux C., et al., 2024, *ApJ*, **960**, L3
- Carter A. L., et al., 2024, *Nature Astronomy*, **8**, 1008
- Chen H., Rogers L. A., 2016, *ApJ*, **831**, 180
- Collier Cameron A., et al., 2019, *MNRAS*, **487**, 1082
- Collins K. A., Kielkopf J. F., Stassun K. G., Hessman F. V., 2017, *AJ*, **153**, 77
- Colome J., Ribas I., 2006, IAU Special Session, **6**, 11
- Colomé J., Casteels K., Ribas I., Francisco X., 2010, in Radziwill N. M., Bridger A., eds, Society of Photo-Optical Instrumentation Engineers (SPIE) Conference Series Vol. 7740, Software and Cyberinfrastructure for Astronomy. p. 77403K, doi:10.1117/12.857672
- Cosentino R., et al., 2012, in McLean I. S., Ramsay S. K., Takami H., eds, Society of Photo-Optical Instrumentation Engineers (SPIE) Conference Series Vol. 8446, Ground-based and Airborne Instrumentation for Astronomy IV. p. 84461V, doi:10.1117/12.925738
- Cowan N. B., Agol E., 2011, *ApJ*, **729**, 54
- Davey J. J., Yip K. H., Al-Refaie A. F., Waldmann I. P., 2025, *MNRAS*, **536**, 2618
- Demangeon O. D. S., et al., 2021, *A&A*, **653**, A41
- Dholakia S., et al., 2024, *MNRAS*, **531**, 1276
- Dressing C. D., Charbonneau D., 2015, *ApJ*, **807**, 45
- Dumusque X., et al., 2021, *A&A*, **648**, A103
- Eastman J., Gaudi B. S., Agol E., 2013, *PASP*, **125**, 83
- Edelson R. A., Krolik J. H., 1988, *ApJ*, **333**, 646
- Egger J. A., et al., 2024, *A&A*, **688**, A223
- Ehrenreich D., et al., 2015, *Nature*, **522**, 459
- Engle S. G., 2024, *ApJ*, **960**, 62
- Engle S. G., Guinan E. F., 2023, *ApJ*, **954**, L50
- Espinoza N., Kossakowski D., Brahm R., 2019, *MNRAS*, **490**, 2262
- Fernández Fernández J., Wheatley P. J., King G. W., 2023, *MNRAS*, **522**, 4251
- Foreman-Mackey D., Hogg D. W., Lang D., Goodman J., 2013, *PASP*, **125**, 306
- Foreman-Mackey D., Agol E., Ambikasaran S., Angus R., 2017, *AJ*, **154**, 220
- Gibson N. P., Aigrain S., Roberts S., Evans T. M., Osborne M., Pont F., 2012, *MNRAS*, **419**, 2683

- Haldemann J., Dorn C., Venturini J., Alibert Y., Benz W., 2024, *A&A*, **681**, A96
- Hoyer S., Guterman P., Demangeon O., Sousa S. G., Deleuil M., Meunier J. C., Benz W., 2020, *A&A*, **635**, A24
- Husser T. O., Wende-von Berg S., Dreizler S., Homeier D., Reiners A., Barman T., Hauschildt P. H., 2013, *A&A*, **553**, A6
- Johnstone C. P., Bartel M., Güdel M., 2021, *A&A*, **649**, A96
- Kempton E. M. R., et al., 2018, *PASP*, **130**, 114401
- Kempton E. M. R., Lessard M., Malik M., Rogers L. A., Futrowsky K. E., Ih J., Marounina N., Romero-Mirza C. E., 2023, *ApJ*, **953**, 57
- Kipping D. M., 2013, *MNRAS*, **435**, 2152
- Kochanek C. S., et al., 2017, *PASP*, **129**, 104502
- Kreidberg L., 2015, *Publications of the Astronomical Society of the Pacific*, **127**, 1161
- Kubyskhina D., et al., 2018, *A&A*, **619**, A151
- Kuzuhara M., et al., 2024, *ApJ*, **967**, L21
- Lafarga M., et al., 2020, *A&A*, **636**, A36
- Linsky J. L., France K., Ayres T., 2013, *ApJ*, **766**, 69
- Malavolta L., et al., 2016, *A&A*, **588**, A118
- Malavolta L., et al., 2018, *AJ*, **155**, 107
- Maxted P. F. L., et al., 2022, *MNRAS*, **514**, 77
- McCully C., Volgenau N. H., Harbeck D.-R., Lister T. A., Saunders E. S., Turner M. L., Siivert R. J., Bowman M., 2018, in *Proc. SPIE*. p. 107070K ([arXiv:1811.04163](https://arxiv.org/abs/1811.04163)), doi:10.1117/12.2314340
- Morello G., Zingales T., Martin-Lagarde M., Gastaud R., Lagage P.-O., 2021, *AJ*, **161**, 174
- Mortier A., 2022, in *The 21st Cambridge Workshop on Cool Stars, Stellar Systems, and the Sun. Cambridge Workshop on Cool Stars, Stellar Systems, and the Sun*. p. 71, doi:10.5281/zenodo.7409757
- Mortier A., Faria J. P., Correia C. M., Santerne A., Santos N. C., 2015, *A&A*, **573**, A101
- Mortier A., et al., 2020, *MNRAS*, **499**, 5004
- Murgas F., et al., 2023, *A&A*, **677**, A182
- Narita N., et al., 2019, *Journal of Astronomical Telescopes, Instruments, and Systems*, **5**, 015001
- Narita N., et al., 2020, in *Evans C. J., Bryant J. J., Motohara K., eds, Society of Photo-Optical Instrumentation Engineers (SPIE) Conference Series Vol. 11447, Ground-based and Airborne Instrumentation for Astronomy VIII*. p. 114475K, doi:10.1117/12.2559947
- Newton E. R., Irwin J., Charbonneau D., Berta-Thompson Z. K., Dittmann J. A., West A. A., 2016, *ApJ*, **821**, 93
- Parc L., Bouchy F., Venturini J., Dorn C., Helled R., 2024, *A&A*, **688**, A59
- Parviainen H., 2015, *MNRAS*, **450**, 3233
- Parviainen H., Aigrain S., 2015, *MNRAS*, **453**, 3821
- Pepe F., et al., 2011, *A&A*, **534**, A58
- Pepe F., et al., 2014, *Astronomische Nachrichten*, **335**, 8
- Pepe F., et al., 2021, *A&A*, **645**, A96
- Perger M., Anglada-Escudé G., Ribas I., Rosich A., Herrero E., Morales J. C., 2021, *A&A*, **645**, A58
- Powell D., et al., 2024, *Nature*, **626**, 979
- Queloz D., et al., 2001, *A&A*, **379**, 279
- Quirrenbach A., et al., 2014, in *Ground-based and Airborne Instrumentation for Astronomy V*. p. 91471F, doi:10.1117/12.2056453
- Quirrenbach A., et al., 2018, in *Ground-based and Airborne Instrumentation for Astronomy VII*. p. 107020W, doi:10.1117/12.2313689
- Rajpaul V., Aigrain S., Osborne M. A., Reece S., Roberts S., 2015, *MNRAS*, **452**, 2269
- Rasmussen C., Williams C., 2010, *the MIT Press*, 122, 935
- Redfield S., Linsky J. L., 2000, *ApJ*, **534**, 825
- Redfield S., et al., 2024, *arXiv e-prints*, p. [arXiv:2404.02932](https://arxiv.org/abs/2404.02932)
- Ricker G., 2021, in *43rd COSPAR Scientific Assembly*. Held 28 January - 4 February. p. 499
- Ricker G. R., et al., 2015, *Journal of Astronomical Telescopes, Instruments, and Systems*, **1**, 014003
- Rogers J. G., Owen J. E., Schlichting H. E., 2024, *MNRAS*, **529**, 2716
- Sabotta S., et al., 2021, *A&A*, **653**, A114
- Shan Y., et al., 2024, *A&A*, **684**, A9
- Shappee B. J., et al., 2014, *ApJ*, **788**, 48
- Shields A. L., Ballard S., Johnson J. A., 2016, *Phys. Rep.*, **663**, 1
- Silva A. M., et al., 2022, *A&A*, **663**, A143
- Stalport M., et al., 2025, *A&A*, **696**, A86
- Tal-Or L., et al., 2018, *A&A*, **614**, A122
- Thiabaud A., Marboeuf U., Alibert Y., Leya I., Mezger K., 2015, *A&A*, **580**, A30
- Trifonov T., et al., 2018, *A&A*, **609**, A117
- Vidal-Madjar A., Lecavelier des Etangs A., Désert J. M., Ballester G. E., Ferlet R., Hébrard G., Mayor M., 2003, *Nature*, **422**, 143
- Waldmann I. P., Tinetti G., Rocchetto M., Barton E. J., Yurchenko S. N., Tennyson J., 2015a, *ApJ*, **802**, 107
- Waldmann I. P., Rocchetto M., Tinetti G., Barton E. J., Yurchenko S. N., Tennyson J., 2015b, *ApJ*, **813**, 13
- Webb N. A., et al., 2020, *A&A*, **641**, A136
- Wilson T. G., et al., 2022, *MNRAS*, **511**, 1043
- Zechmeister M., Kürster M., 2009, *A&A*, **496**, 577
- Zechmeister M., Anglada-Escudé G., Reiners A., 2014, *A&A*, **561**, A59
- Zechmeister M., et al., 2018, *A&A*, **609**, A12
- Zeng L., et al., 2019, *Proceedings of the National Academy of Science*, **116**, 9723

<sup>1</sup>School of Physics and Astronomy, University of Birmingham, Edgbaston, Birmingham B15 2TT, UK

<sup>2</sup>Department of Physics, University of Warwick, Gibbet Hill Road, Coventry, CV4 7LS, UK

<sup>3</sup>Instituto de Astrofísica de Canarias (IAC), 38205 La Laguna, Tenerife, Spain

<sup>4</sup>Departamento de Astrofísica, Universidad de La Laguna (ULL), 38206 La Laguna, Tenerife, Spain

<sup>5</sup>Instituto de Astrofísica de Andalucía (IAA), 18080, Granada, Spain

<sup>6</sup>INAF – Osservatorio Astronomico di Palermo, Piazza del Parlamento, 1, 90134 Palermo, Italy

<sup>7</sup>Carnegie Science Observatories, 813 Santa Barbara Street, Pasadena, CA 91101, USA

<sup>8</sup>Centro de Astrobiología, CSIC-INTA, Camino Bajo del Castillo s/n, Villanueva de la Cañada, Madrid

<sup>9</sup>Institut für Astrophysik und Geophysik, Georg-August-Universität, Friedrich-Hund-Platz 1, 37077 Göttingen, Germany

<sup>10</sup>Space Research and Planetary Sciences, Physics Institute, University of Bern, Gesellschaftsstrasse 6, 3012 Bern, Switzerland

<sup>11</sup>Department of Physics & Astronomy, McMaster University, 1280 Main St W, Hamilton, ON, L8S 4L8, Canada

<sup>12</sup>Thüringer Landessternwarte Tautenburg, Germany

<sup>13</sup>INAF – Osservatorio Astrofisico di Torino, Via Osservatorio 20, 10025 Pino Torinese, Italy

<sup>14</sup>Institut de Ciències de l’Espai (ICE, CSIC), Campus UAB, Can Magrans s/n, 08193 Bellaterra, Spain

<sup>15</sup>Institut d’Estudis Espacials de Catalunya (IEEC), 08860 Castelldefels (Barcelona), Spain

<sup>16</sup>Vereinigting Voor Sterrenkunde (VVS), Oostmeers 122 C, 8000 Brugge, Belgium

<sup>17</sup>Public observatory ASTROLAB IRIS, Provinciaal Domein “De Palingbeek”, Verbrandemolenstraat 5, 8902 Zillebeke, Ieper, Belgium

<sup>18</sup>Centre for Astrophysics, University of Southern Queensland, Toowoomba, QLD 4350, Australia

<sup>19</sup>DTU Space, Technical University of Denmark, Elektrovej 328, DK-2800 Kgs. Lyngby, Denmark

<sup>20</sup>SUPA School of Physics and Astronomy, University of St Andrews, North Haugh, St Andrews, KY16 9SS, UK

<sup>21</sup>Tata Institute of Fundamental Research, Mumbai, India

<sup>22</sup>Department of Physics, Ariel University, Ariel 40700, Israel

<sup>23</sup>Observatoire Astronomique de l'Université de Genève, Chemin Pegasi 51, CH-1290 Versoix, Switzerland

<sup>24</sup>Fundación Galileo Galilei - INAF, Rambla José Ana Fernández Pérez 7, E-38712 Breña Baja, Tenerife, Spain

<sup>25</sup>Space Telescope Science Institute, 3700 San Martin Drive, Baltimore, MD 20218, USA <sup>26</sup>Dipartimento di Fisica e Astronomia "Galileo Galilei", Università di Padova, Vicolo dell'Osservatorio 3, 35122, Padova, Italy

<sup>27</sup>Istituto Nazionale di Astrofisica – Osservatorio Astronomico di Padova, Vicolo dell'Osservatorio 5, 35122, Padova, Italy

<sup>28</sup>Department of Physics, University of Rome "Tor Vergata", Via della Ricerca Scientifica 1 I-00133 Roma, Italy

<sup>29</sup>Departamento de Física de la Tierra y Astrofísica and IPARCOS-UCM (Instituto de Física de Partículas y del Cosmos de la UCM), Facultad de Ciencias Físicas, Universidad Complutense de Madrid, E-28040, Madrid, Spain

<sup>30</sup>Department of Astronomy, University of Texas at Austin, 2515 Speedway, Austin, TX 78712, USA

<sup>31</sup>SUPA, Institute for Astronomy, University of Edinburgh, Blackford Hill, Edinburgh, EH9 3HJ, UK

<sup>32</sup>Centre for Exoplanet Science, University of Edinburgh, Edinburgh, EH9 3HJ, UK

<sup>33</sup>Landessternwarte, Zentrum für Astronomie der Universität Heidelberg, Königstuhl 12, 69117 Heidelberg, Germany

<sup>34</sup>Instituto de Astrofísica e Ciências do Espaço, CAUP, Universidade do Porto, Rua das Estrelas, 4150-762 Porto, Portugal

<sup>35</sup>Departamento de Física e Astronomia, Faculdade de Ciências, Universidade do Porto, Rua do Campo Alegre, 4169-007 Porto, Portugal

<sup>36</sup>Space sciences, Technologies and Astrophysics Research (STAR) Institute, Université de Liège, Allée du 6 Août 19C, 4000 Liège, Belgium

<sup>37</sup>Astrobiology Research Unit, Université de Liège, Allée du 6 Août 19C, B-4000 Liège, Belgium

<sup>38</sup>Astrophysics, Geophysics, And Space Science Research Center, Ariel University, Ariel 40700, Israel

<sup>39</sup>Department of Astronomy, Faculty of Physics, Sofia University "St Kliment Ohridski", 5 James Bourchier Blvd, 1164 Sofia, Bulgaria

## APPENDIX A: LONG-TERM PHOTOMETRY

Figure A1 shows the long-term photometry used in Section 3.1 to determine the stellar rotation period.

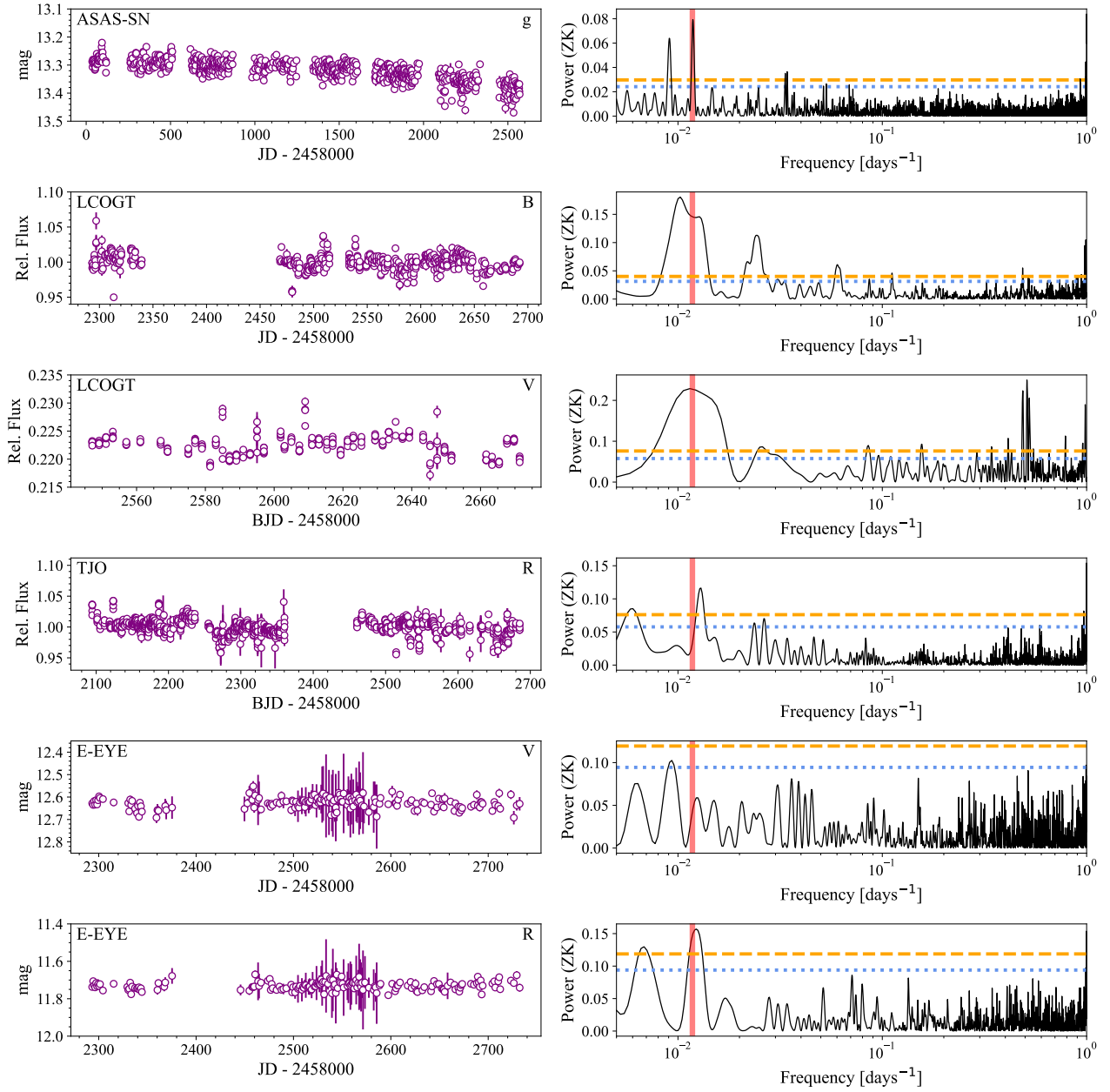
## APPENDIX B: RV PERIODOGRAMS

Figure B1 shows the periodograms for the RV and H  $\alpha$  time series for HARPS-N, ESPRESSO, and CARMENES.

## APPENDIX C: PRIORS AND FITTED PARAMETERS

Tables C1 and C2 show the prior distributions used during the different fitting procedures. Table C3 has the final fitted values related to the star as well as the various instruments.

This paper has been typeset from a  $\text{\TeX}/\text{\LaTeX}$  file prepared by the author.



**Figure A1.** Gliese 12 long-term ground-based photometry and GLS periodograms (Zechmeister & Kürster 2009) of the time series. The vertical red line marks the rotation period  $P_{\text{rot}} = 85$  d presented in Kuzuhara et al. (2024), the horizontal lines represent the 10 per cent (blue) and 1 per cent (orange) false alarm probability levels.

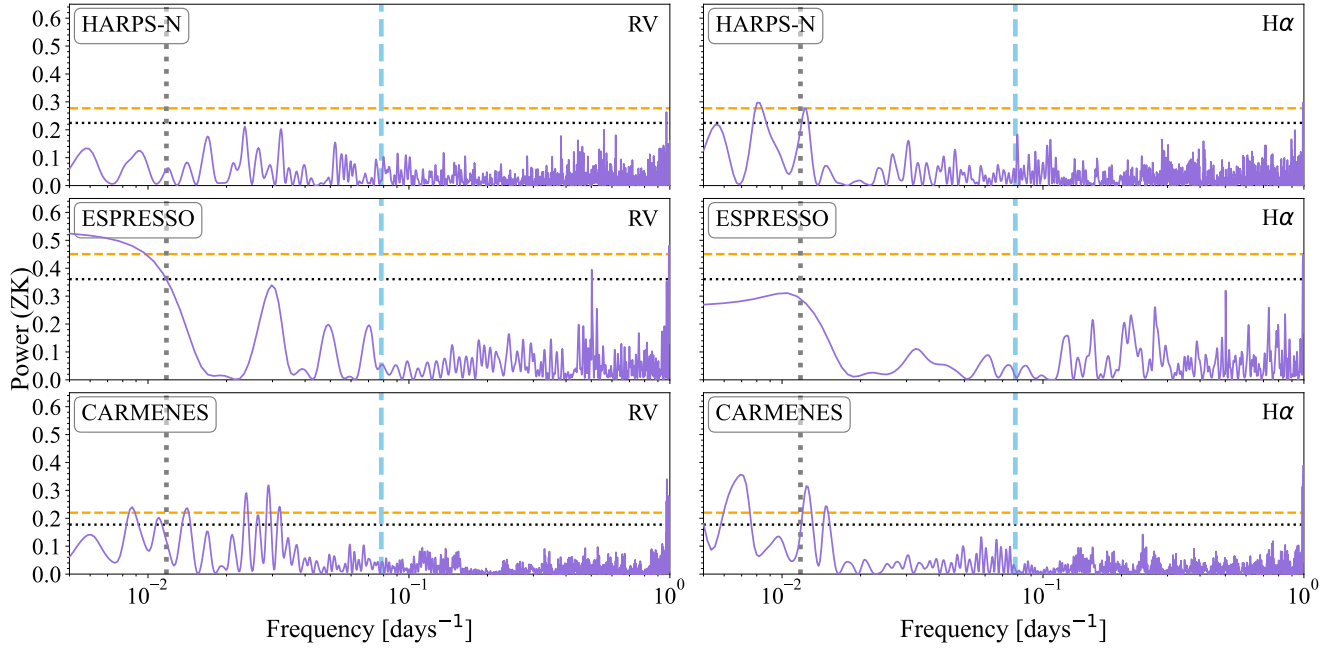


**Figure B1.** GLS periodograms for the RV and  $H\alpha$  data from all three instruments. The vertical lines in the plot are the orbital period of Gliese 12 b (dashed light blue line,  $P = 12.7614$  d), and  $P_{\text{rot}} = 85$  d (gray dotted line). The horizontal lines are the false alarm probabilities (FAP) = 10 per cent (black dotted line) and 1 per cent (dashed orange line).

**Table C1.** Priors for the planet parameters

Parameter	Unit	Photometry-only fit	Informed RV fit	Joint fit
$P$	(d)	$\mathcal{N}(12.761408, 0.1)$	$\mathcal{N}(12.761422, 0.000047)$	$\mathcal{U}(12.46, 13.06)$
$T_0$	(BJD)	$\mathcal{N}(2459497.1865, 0.1)$	$\mathcal{N}(2460492.5747, 0.0044)$	$\mathcal{U}(2460032.86, 2460033.46)$
$R_p/R_\star$	—	$\mathcal{U}(0, 1)$	—	$\mathcal{U}(0.0, 0.5)$
$b$	—	$\mathcal{U}(0, 1)$	—	$\mathcal{U}(0, 1)$
$\rho_\star$	( $\text{g cm}^{-3}$ )	$\mathcal{N}(18.9879198, 15.950938)$	—	$\mathcal{N}(18.96576, 15.9104)$
$K$	( $\text{m s}^{-1}$ )	—	$\mathcal{U}(0, 2.5)$	$\mathcal{U}(0, 50)$
$\sqrt{e} \sin \omega$	—	—	$\mathcal{U}(-1, 1)$	$\mathcal{U}(-1, 1)$
$\sqrt{e} \cos \omega$	—	—	$\mathcal{U}(-1, 1)$	$\mathcal{U}(-1, 1)$
$e$	—	$\mathcal{U}(0, 0.9)$	—	$\mathcal{U}(0.0, 0.95)$
$\omega$	(deg)	$\mathcal{U}(0, 360)$	—	$\mathcal{U}(0, 360)$

**Table C2.** Stellar and instrumental priors. We note that the coherence GP parameter is different for both fits due to a different functional form of the same kernel.

Parameter	Unit	Photometry-only fit	Informed RV fit	Joint fit
$P_{\text{rot,GP}}$	(d)	—	$\mathcal{U}(25, 200)$	$\mathcal{U}(60, 200)$
coherence	—	—	$\lambda_p \in \mathcal{U}(0.01, 10)$	$w \in \mathcal{U}(0.001, 3.0)$
evolution	(d)	—	$\lambda_e \in \mathcal{U}(5, 1000)$	$\lambda \in \mathcal{U}(120.0, 1000.0)$
amplitude	(m s <sup>-1</sup> )	—	$A_0 \in \mathcal{U}(0, 10)$	$H, C \in \mathcal{U}(0, 50)$
jitter HN	(m s <sup>-1</sup> )	—	$\mathcal{U}(0, 100)$	$\mathcal{U}(0.01, 256)$
jitter CARM	(m s <sup>-1</sup> )	—	$\mathcal{U}(0, 100)$	$\mathcal{U}(0.01, 312)$
jitter ESPR	(m s <sup>-1</sup> )	—	$\mathcal{U}(0, 100)$	$\mathcal{U}(0.02, 57)$
offset HN	(m s <sup>-1</sup> )	—	$\mathcal{U}(51230.45, 51446.16)$	$\mathcal{U}(-10000, 10000)$
offset CARM	(m s <sup>-1</sup> )	—	$\mathcal{U}(51305.26, 51513.63)$	$\mathcal{U}(-10000, 10000)$
offset ESPR	(m s <sup>-1</sup> )	—	$\mathcal{U}(-106.67, 105.88)$	$\mathcal{U}(-10000, 10000)$
GP $_{\sigma}$	(ppm)	—	—	$\log_{10}(\mathcal{U}(-6, 6))$
GP $_{\rho}$	(d)	—	—	$\log_{10}(\mathcal{U}(-3, 3))$
LD TESS		$q_1 \in \mathcal{U}(0, 1.0)$	—	$u_1 \in \mathcal{N}(0.26, 0.05)$
LD TESS		$q_2 \in \mathcal{U}(0, 1.0)$	—	$u_2 \in \mathcal{N}(0.30, 0.10)$
LD CHEOPS		$q_1 \in \mathcal{U}(0, 1.0)$	—	$u_1 \in \mathcal{N}(0.26, 0.04)$
LD CHEOPS		$q_2 \in \mathcal{U}(0, 1.0)$	—	$u_2 \in \mathcal{N}(0.28, 0.09)$
LD MuSCAT2 $r$		$q_1 \in \mathcal{U}(0, 1.0)$	—	—
LD MuSCAT2 $r$		$q_2 \in \mathcal{U}(0, 1.0)$	—	—
LD MuSCAT3 $r$		$q_1 \in \mathcal{U}(0, 1.0)$	—	—
LD MuSCAT3 $r$		$q_2 \in \mathcal{U}(0, 1.0)$	—	—
LD MuSCAT2 $i$		$q_1 \in \mathcal{U}(0, 1.0)$	—	—
LD MuSCAT2 $i$		$q_2 \in \mathcal{U}(0, 1.0)$	—	—
LD MuSCAT3 $i$		$q_1 \in \mathcal{U}(0, 1.0)$	—	—
LD MuSCAT3 $i$		$q_2 \in \mathcal{U}(0, 1.0)$	—	—
LD MuSCAT2 $z$		$q_1 \in \mathcal{U}(0, 1.0)$	—	—
LD MuSCAT2 $z$		$q_2 \in \mathcal{U}(0, 1.0)$	—	—
LD MuSCAT3 $z$		$q_1 \in \mathcal{U}(0, 1.0)$	—	—
LD MuSCAT3 $z$		$q_2 \in \mathcal{U}(0, 1.0)$	—	—
offset TESS		$\mathcal{N}(0, 0.1)$	—	—
offset CHEOPS		$\mathcal{N}(0, 0.1)$	—	—
offset MuSCAT2 $r$		$\mathcal{N}(0, 0.1)$	—	—
offset MuSCAT3 $r$		$\mathcal{N}(0, 0.1)$	—	—
offset MuSCAT2 $i$		$\mathcal{N}(0, 0.1)$	—	—
offset MuSCAT3 $i$		$\mathcal{N}(0, 0.1)$	—	—
offset MuSCAT2 $z$		$\mathcal{N}(0, 0.1)$	—	—
offset MuSCAT3 $z$		$\mathcal{N}(0, 0.1)$	—	—
jitter TESS	(ppm)	$\mathcal{L}(0.1, 1000.0)$	—	$\mathcal{U}(0, 119800); \mathcal{U}(0, 117600); \mathcal{U}(0, 118000); \mathcal{U}(0, 117600);$ $\mathcal{U}(0, 128000); \mathcal{U}(0, 128500); \mathcal{U}(0, 121600); \mathcal{U}(0, 121100)$
jitter CHEOPS	(ppm)	$\mathcal{L}(0.1, 100000.0)$	—	$\mathcal{U}(0, 69800); \mathcal{U}(0, 62700); \mathcal{U}(0, 67000); \mathcal{U}(0, 63000);$ $\mathcal{U}(0, 62800); \mathcal{U}(0, 251000)$
jitter MuSCAT2 $r$	(ppm)	$\mathcal{L}(0.1, 100000.0)$	—	—
jitter MuSCAT3 $r$	(ppm)	$\mathcal{L}(0.1, 100000.0)$	—	—
jitter MuSCAT2 $i$	(ppm)	$\mathcal{L}(0.1, 100000.0)$	—	—
jitter MuSCAT3 $i$	(ppm)	$\mathcal{L}(0.1, 100000.0)$	—	—
jitter MuSCAT2 $z$	(ppm)	$\mathcal{L}(0.1, 100000.0)$	—	—
jitter MuSCAT3 $z$	(ppm)	$\mathcal{L}(0.1, 100000.0)$	—	—

**Table C3.** Stellar and instrumental parameters. We note that the coherence GP parameter is different for both fits due to a different functional form of the same kernel.

Parameter	Unit	Photometry-only fit	Informed RV fit	Joint fit
$P_{\text{rot,GP}}$	(d)	—	$121.6^{+51.5}_{-61.8}$	$171.9^{+1.6}_{-1.7}$
coherence	—	—	$\lambda_p = 3.10^{+4.64}_{-2.87}$	$w = 0.212^{+0.056}_{-0.047}$
evolution	(d)	—	$\lambda_e = 9.61^{+56.53}_{-2.06}$	$\lambda = 476^{+262}_{-159}$
amplitude	( $\text{m s}^{-1}$ )	—	$A_0 = 2.04^{+0.44}_{-0.34}$	$H_{\text{HN}} = 2.10^{+0.92}_{-0.68}$ ; $H_{\text{CARM}} = 2.51^{+1.20}_{-0.74}$ ; $H_{\text{ESPR}} = 0.84^{+0.18}_{-0.15}$ $C_{\text{HN}} = 0.77^{+1.10}_{-0.55}$ ; $C_{\text{CARM}} = 1.07^{+1.60}_{-0.76}$ ; $C_{\text{ESPR}} = 2.2^{+5.0}_{-1.6}$
jitter HN	( $\text{m s}^{-1}$ )	—	$1.37^{+0.32}_{-0.31}$	$1.77^{+0.36}_{-0.33}$
jitter CARM	( $\text{m s}^{-1}$ )	—	$0.25^{+0.29}_{-0.18}$	$0.35^{+0.35}_{-0.24}$
jitter ESPR	( $\text{m s}^{-1}$ )	—	$0.84^{+0.18}_{-0.14}$	$0.84^{+0.18}_{-0.15}$
offset HN	( $\text{m s}^{-1}$ )	—	$51337.25 \pm 0.56$	$-0.06^{+0.94}_{-0.91}$
offset CARM	( $\text{m s}^{-1}$ )	—	$0.47^{+0.56}_{-0.54}$	$0.10^{+1.20}_{-1.00}$
offset ESPR	( $\text{m s}^{-1}$ )	—	$51409.56^{+0.59}_{-0.58}$	$0.20^{+1.60}_{-1.30}$
LD TESS		$q_1 = 0.39^{+0.30}_{-0.23}$	—	$u_1 = 0.26^{+0.05}_{-0.05}$
LD TESS		$q_2 = 0.29^{+0.22}_{-0.18}$	—	$u_2 = 0.30^{+0.10}_{-0.10}$
LD CHEOPS		$q_1 = 0.18^{+0.19}_{-0.13}$	—	$u_1 = 0.26^{+0.04}_{-0.04}$
LD CHEOPS		$q_2 = 0.37^{+0.28}_{-0.22}$	—	$u_2 = 0.28^{+0.09}_{-0.09}$
LD MuSCAT2 <i>r</i>		$q_1 = 0.23^{+0.26}_{-0.16}$	—	—
LD MuSCAT2 <i>r</i>		$q_2 = 0.42^{+0.30}_{-0.27}$	—	—
LD MuSCAT3 <i>r</i>		$q_1 = 0.45^{+0.25}_{-0.22}$	—	—
LD MuSCAT3 <i>r</i>		$q_2 = 0.57^{+0.25}_{-0.26}$	—	—
LD MuSCAT2 <i>i</i>		$q_1 = 0.43^{+0.23}_{-0.24}$	—	—
LD MuSCAT2 <i>i</i>		$q_2 = 0.36^{+0.32}_{-0.24}$	—	—
LD MuSCAT3 <i>i</i>		$q_1 = 0.47^{+0.25}_{-0.24}$	—	—
LD MuSCAT3 <i>i</i>		$q_2 = 0.29^{+0.28}_{-0.20}$	—	—
LD MuSCAT2 <i>z</i>		$q_1 = 0.23^{+0.28}_{-0.16}$	—	—
LD MuSCAT2 <i>z</i>		$q_2 = 0.40^{+0.32}_{-0.26}$	—	—
LD MuSCAT3 <i>z</i>		$q_1 = 0.49^{+0.23}_{-0.23}$	—	—
LD MuSCAT3 <i>z</i>		$q_2 = 0.40^{+0.29}_{-0.25}$	—	—
offset TESS		$0.000003^{+0.000021}_{-0.000021}$	—	—
offset CHEOPS		$0.000163^{+0.000017}_{-0.000018}$	—	—
offset MuSCAT2 <i>r</i>		$0.000419^{+0.000050}_{-0.000046}$	—	—
offset MuSCAT3 <i>r</i>		$0.000017^{+0.000031}_{-0.000031}$	—	—
offset MuSCAT2 <i>i</i>		$0.000022^{+0.000035}_{-0.000034}$	—	—
offset MuSCAT3 <i>i</i>		$0.000032^{+0.000032}_{-0.000034}$	—	—
offset MuSCAT2 <i>z</i>		$0.000050^{+0.000043}_{-0.000044}$	—	—
offset MuSCAT3 <i>z</i>		$0.000012^{+0.000032}_{-0.000034}$	—	—
jitter TESS	(ppm)	$1.05^{+5.20}_{-0.81}$	—	$114^{+100}_{-72}$ ; $102^{+93}_{-64}$ ; $390^{+110}_{-150}$ ; $132^{+100}_{-72}$ ; $160^{+130}_{-100}$ ; $104^{+96}_{-64}$ ; $99^{+91}_{-61}$ ; $122^{+110}_{-76}$
jitter CHEOPS	(ppm)	$0.621^{+0.075}_{-0.071}$	—	$380^{+49}_{-52}$ ; $434^{+47}_{-48}$ ; $355^{+75}_{-83}$ ; $670^{+69}_{-66}$ ; $205^{+96}_{-110}$ ; $160^{+160}_{-100}$
jitter MuSCAT2 <i>r</i>	(ppm)	$784.91^{+51.39}_{-49.42}$	—	—
jitter MuSCAT3 <i>r</i>	(ppm)	$599.73^{+46.93}_{-51.95}$	—	—
jitter MuSCAT2 <i>i</i>	(ppm)	$1216.67^{+40.25}_{-39.34}$	—	—
jitter MuSCAT3 <i>i</i>	(ppm)	$552.04^{+71.16}_{-84.80}$	—	—
jitter MuSCAT2 <i>z</i>	(ppm)	$1335.90^{+48.65}_{-44.54}$	—	—
jitter MuSCAT3 <i>z</i>	(ppm)	$405.06^{+156.39}_{-383.93}$	—	—